
ROBUST ESTIMATION OF STRUCTURAL ORIENTATION PARAMETERS AND 2D/3D LOCAL ANISOTROPIC TIKHONOV REGULARIZATION

A PREPRINT

Ali Gholami

Institute of Geophysics, Polish Academy of Sciences, Warsaw, Poland
agholami@igf.edu.pl

Silvia Gazzola

Department of Mathematical Sciences, University of Bath, Bath, UK
S.Gazzola@bath.ac.uk

September 10, 2024

ABSTRACT

Understanding the orientation of geological structures is crucial for analyzing the complexity of the Earth's subsurface. For instance, information about geological structure orientation can be incorporated into local anisotropic regularization methods as a valuable tool to stabilize the solution of inverse problems and produce geologically plausible solutions. We introduce a new variational method that employs the alternating direction method of multipliers within an alternating minimization scheme to jointly estimate orientation and model parameters in both 2D and 3D inverse problems. Specifically, the proposed approach adaptively integrates recovered information about structural orientation, enhancing the effectiveness of anisotropic Tikhonov regularization in recovering geophysical parameters. The paper also discusses the automatic tuning of algorithmic parameters to maximize the new method's performance. The proposed algorithm is tested across diverse 2D and 3D examples, including structure-oriented denoising and trace interpolation. The results show that the algorithm is robust in solving the considered large and challenging problems, alongside efficiently estimating the associated tilt field in 2D cases and the dip, strike, and tilt fields in 3D cases. Synthetic and field examples show that the proposed anisotropic regularization method produces a model with enhanced resolution and provides a more accurate representation of the true structures.

1 Introduction

Determining the orientation of geological structures is critical for estimating the complex characteristics of the Earth's subsurface. These key orientation parameters, including attributes like dip, strike, and tilt angles, are instrumental in revealing the nature of both linear and planar geological formations hidden beneath the Earth's surface. Such insights form the foundation for a wide range of geoscientific applications, including data processing, imaging, and interpretation. These applications perform critical tasks such as velocity analysis, velocity-independent time-domain seismic imaging, spatial data interpolation, deblending of simultaneous source data, and fault detection [5, 12, 17, 20, 25, 28, 29, 32, 34].

Advanced technologies, including sophisticated data processing techniques, are used to reveal the complex nature of underground formations. Many of these processes manifest as discrete ill-posed inverse problems, as extensively documented in publications [1, 22, 31]. When solving the inverse problem, anisotropic regularization is pivotal in computing solutions that integrate observed data with physical models while remaining geologically reasonable. Namely, such methods stabilize the solution by imposing regularization that depends on (an estimate of) the (local) orientation of the solution. If correct (prior) information about the orientation of structures contained in the model to be estimated

is included in the regularizer, then oriented structures such as faults and steeply sloping features are suitably recovered, preventing coherent events from smearing normal to the structures.

Denosing is an important step in many data processing, inversion, and interpretation tasks. It is used to increase the desired information content of the input signal by rejecting the unwanted part, namely noise. A nonlinear structure-oriented filter was developed for this purpose in studies conducted by Bakker et al. [2] and Hale [20]. This filter follows a two-step process: initially, structure tensors are computed, and then an anisotropic filter is designed to apply smoothing in an anisotropic manner. An important component of anisotropic smoothers is the availability of an accurate local structural orientation field used to determine the correct direction for smoothing [see, e.g., 12, 17, 20, 25, 32].

In two-dimensional (2D) problems, local tilt information can be extracted directly from the data, e.g., by filtering schemes [2, 27]. Based on the plane wave destruction algorithm [10], Fomel [15] has proposed an algorithm for estimating local event tilts/slopes directly from the data. In this approach, the tilt field appears as coefficients of plane wave prediction filters formulated as a nonlinear optimization problem in the z-transform domain and solved by the Gauss-Newton method. Fomel’s algorithm has been studied and improved by a number of researchers [6, 7, 29]. A major task in performing the algorithm is to stabilize the filter to mitigate sensitivity to noise in the input data [4]. To address this issue, a smoothing filter may be used in a preprocessing step to clean the input data to a certain degree before using it for the subsequent tilt estimation [32].

Traditional filter-based algorithms for local tilt estimation can be effective for calculating the tilt field from direct measurements. However, they encounter challenges when dealing with indirect measurements where the data space does not match the model space [13]. In such cases, well-log information or preprocessed data that are mapped into the model space, such as stacked or migrated sections, are used in [12] to compute the local tilt field. Subsequently, anisotropic Tikhonov regularization is applied to solve tomographic problems.

If information about the local tilt is available, a rotation matrix can be applied to the gradient components (horizontal and vertical derivatives) of the model so that the directional derivative along the local tilt is obtained. The application of Tikhonov regularization with a regularization term defined with respect to the rotated gradient evaluated in a specific norm favors solutions that have elongated features along the specified tilt angle [25, 33]. The plane-wave construction method may be used to force such features based on a model reparameterization [17].

In this paper, we develop a variational framework, i.e., an optimization problem, for jointly estimating the model parameters (sometimes also referred to as the “signal”) and the corresponding local orientation field. The basic assumption underlying the proposed method is that a weighted norm of the directional derivative of a signal is minimal when computed along the true local signal orientation. Therefore, in 2D space, given a clean signal, the local tilt field can be determined by minimizing a weighted norm of the directional derivative of the signal with respect to the local tilt field, defined between $-\pi/2$ and $\pi/2$. However, the solution is not unique in constant regions. By assuming that the signal orientation is locally stationary, we add a regularization term to the objective function to enforce the smooth variation of the tilt field. This leads to a box-constrained nonlinear minimization problem, which is efficiently solved by the alternating direction method of multipliers (ADMM) [3, 18, 30]. If the input signal is noisy or the data space does not match the model space, we solve the problem for the clean signal and the associated tilt field simultaneously using an alternating minimization approach. Specifically, given an initial tilt estimate, the clean signal is recovered through local anisotropic Tikhonov regularization defined with respect to the current tilt field estimate. The Tikhonov regularization parameter, which balances the contribution of the fit-to-data term and the regularization term, is chosen according to the discrepancy principle, so that the restored signal fits the data up to some tolerance given by the norm of the noise in the data. In this way, we look for a clean signal that is close to the noisy signal but, thanks to the regularization term, has minimal fluctuations along the specified, smoothly varying local tilts. The tilt field is then updated as described above, taking as the clean signal the current estimate thereof. This process of alternating between tilt field and signal updates is repeated until a stopping criterion is satisfied.

Specifying orientation in three-dimensional (3D) space is more difficult than in 2D space, where orientation can be defined by a single tilt parameter. We are interested in determining both linear and planar features in 3D models that can be completely specified by three angles: dip, strike, and tilt. A weighted norm of the directional derivatives in two orthogonal directions is minimized to determine these angles. Similarly to the 2D case, we propose 3D regularization functions that are structure adaptive and can properly regularize 3D inverse problems based on this information. The ADMM is used to minimize the objective function while simultaneously estimating the model and orientation parameters.

Although in this paper we are interested only in the regularized output of our 2D and 3D algorithms, the estimated orientation parameters also can be used as a side-product for other purposes. For example, the orientation parameters

have important seismic applications for interpretation and imaging (see, e.g., Fomel [16], Marfurt [27], Merzlikin et al. [28], Schleicher et al. [29], Wu and Janson [34]).

The main contributions of this work can be summarized as follows:

1. We introduce a novel optimization problem designed for the estimation of local orientation fields, including tilt in 2D signals and dip, strike, and tilt in 3D signals. Additionally, we present an efficient computational algorithm adapted to solve this optimization problem.
2. We propose an algorithm that, through an alternating minimization strategy, naturally incorporates the newly developed local orientation estimation scheme (tailored to address 2D and 3D geophysical inverse problems) into the framework of adaptive anisotropic regularization.
3. We apply the formulated algorithms to geophysical applications, specifically focusing on denoising and trace interpolation. The results obtained from these applications demonstrate the practical utility and effectiveness of the algorithm in tackling large-scale and challenging data processing problems.

The rest of the paper is organized as follows. First, assuming local tilt information is available, we present the local anisotropic Tikhonov regularization method for 2D problems. We then set up an optimization problem that allows for the simultaneous estimation of local tilts and model parameters, and we explain how it can be solved using alternating minimization and ADMM. Then we extend our method to 3D problems and show some experimental results for the 2D and 3D cases. We end with some concluding remarks.

2 2D Anisotropic regularization

In the 2D case, the model parameters vector m , representing a quantity of interest, is obtained by stacking the columns of a rectangular $N_z \times N_x$ array such that its length N is given by the product $N_z N_x$. In various steps of data processing and imaging, such models may appear as the solution of ill-conditioned linear systems of equations of the form

$$d = Gm + e, \quad (1)$$

where d and e are real vectors of length M representing known measured data and unknown white Gaussian noise, respectively, the unknown m is a real vector of length N , and G is the linear forward operator from the model space to the data space [1, 22, 31]. Due to the presence of noise and the typical ill-conditioning of the system, a suitable regularization is required to produce a reasonable estimate of the model. Tikhonov regularization defines m as the solution of the following optimization problem:

$$\min_m \frac{\mu}{2} \|Gm - d\|_2^2 + \frac{1}{2} \sum_{i=1}^N \|(\nabla m)_i\|_2^2, \quad (2)$$

where the penalty parameter μ balances the action of the data fit against regularization, $\|\cdot\|_2$ denotes the vector 2-norm, and ∇ is a scaled discrete gradient operator. We recall that $(\nabla m)_i$ is a two-component vector of the form

$$(\nabla m)_i = \begin{bmatrix} (\nabla_x m)_i \\ (\nabla_z m)_i \end{bmatrix}, \quad (3)$$

where ∇_x and ∇_z are finite difference operators discretizing the first-order horizontal (x) and vertical (z) derivatives. A main issue of the Tikhonov regularizer is that it is homogeneous, in the sense that it does not take into account the structure of the regularized solution and therefore tends to over-smooth the model. One possible way to overcome this problem is to implement anisotropic regularization by penalizing directional derivatives. This can be done by rotating and scaling the gradient vector in the regularization function as follows:

$$\sum_{i=1}^N \|R(\theta_i)(\nabla m)_i\|_{\Sigma_i}^2, \quad (4)$$

where

$$R(\theta_i) = \begin{pmatrix} \cos \theta_i & \sin \theta_i \\ -\sin \theta_i & \cos \theta_i \end{pmatrix} := \begin{pmatrix} x'(\theta_i) \\ z'(\theta_i) \end{pmatrix}, \quad (5)$$

and $\Sigma_i = \begin{pmatrix} \sigma_x & 0 \\ 0 & \sigma_z \end{pmatrix}$. Here and below, $\theta_i \in (-\frac{\pi}{2}, \frac{\pi}{2}]$ is the local signal tilt angle (orientation) which is measured clockwise about the origin (see Figure 1), R is a rotation matrix that converts any coordinates in the original (x, z)

system into (x', z') coordinates defined in terms of θ_i , and $\|g\|_{\Sigma_i}^2 = g^T \Sigma_i g$ denotes the weighted vector 2-norm with weighting matrix Σ_i that weights the rotated gradient components by the coefficients $\sigma_x \geq \sigma_z \geq 0$. This weighting allows for flexible smoothing of the signal in the tilt direction relative to the orthogonal one, as well as control over the anisotropic behavior of the regularization. For $\sigma_z = 0$, no smoothing orthogonal to the θ_i direction is applied. The regularization in this case is maximally anisotropic and favors models with elongated features along the structure direction θ_i . In general, σ_x and σ_z can be adjusted locally for each model point [24]. However, for the sake of simplicity, we will use fixed values in this paper (so that $\Sigma_i = \Sigma$). In this case, without loss of generality we set $\sigma_x = 1$ and $\sigma_z = \epsilon$ with $\epsilon \ll 1$, forcing line-like linear structures in the final model.

As stated in the Introduction, our approach to estimating the tilt field hinges on a fundamental hypothesis: an estimate of the tilt field for a 2D model can be obtained by minimizing a weighted norm of the directional derivative defined with respect to such tilt field. In Appendix A, we show that this is true for a simple 2D sinusoidal plane wave.

In general, given an initial guess θ for the tilt field, we propose an iterative method that simultaneously estimates both the tilt field and model parameters by the following two-step alternating minimization scheme

$$m^+ = \operatorname{argmin}_m \frac{\mu}{2} \|Gm - d\|_2^2 + \frac{1}{2} \sum_{i=1}^N \|R(\theta_i)(\nabla m)_i\|_{\Sigma}^2, \quad (6)$$

$$\theta^+ = \operatorname{argmin}_{\theta \in B} \frac{1}{2} \sum_{i=1}^N \|R(\theta_i)(\tilde{\nabla} m^+)_i\|_{\Sigma}^2 + \frac{\rho}{2} \|\nabla \theta\|_2^2, \quad (7)$$

where θ^+ is the updated tilt associated with the updated model parameters m^+ . Specifically, at each iteration of the above scheme, the first subproblem in equation 6 involves the estimation of the model parameters by local anisotropic Tikhonov regularization, given the most recent tilt field θ , while the second subproblem in equation 7 involves the update of the tilt field based on the most recently estimated model m^+ . Here, $B = \{\theta \in \mathbb{R}^N : -\frac{\pi}{2} < \theta \leq \frac{\pi}{2}\}$ and $\rho > 0$ is a positive parameter controlling the smoothness of the estimated tilt field. In equation 7, $\tilde{\nabla} m$ represents a smoothed (regularized) estimate of the model gradient ∇m . We achieve this by smoothing the gradient components using smooth derivative filters h_x and h_z , i.e.

$$\tilde{m}_x := \tilde{\nabla}_x m = h_x \star m, \quad \tilde{m}_z := \tilde{\nabla}_z m = h_z \star m, \quad (8)$$

where \star denotes the 2D convolution operator. These filters, for the conventional first-order finite difference approximation (without smoothing), are defined as:

$$h_x = \begin{bmatrix} \frac{1}{2} & 0 & -\frac{1}{2} \end{bmatrix}, \quad h_z = \begin{bmatrix} \frac{1}{2} & 0 & -\frac{1}{2} \end{bmatrix}^T. \quad (9)$$

While these filters provide a critical 90° phase shift that facilitates orientation determination, they also introduce unwanted amplitude scaling issues. To mitigate these instabilities and obtain a stable estimate of signal variations, we remove the frequency-dependent amplitude scaling from the derivatives. For this purpose, we employ the Hilbert transform, known for its 90° phase shift property akin to derivatives but without altering amplitudes [9]. The associated filters are defined as [14]:

$$h_x = -\frac{1}{2\pi} \frac{x}{(x^2 + z^2)^{3/2}}, \quad h_z = -\frac{1}{2\pi} \frac{z}{(x^2 + z^2)^{3/2}}. \quad (10)$$

These filters are illustrated in Figure 2. They represent a smoothed version of the differentiators in equation 9. To show the performance of these filters, we present a comparison in Figure 3. A sinusoidal plane wave both with and without added random noise is shown in Figure 3a and b, respectively. We computed the horizontal derivative of the signal obtained using the Hilbert transform filter (Figure 3c and d) and the standard finite differences method (Figure 3e and f). We observe that, the Hilbert transform filter exhibits greater stability in the presence of noise.

2.1 Solving the Model Subproblem in equation 6

We first note that

$$\sum_{i=1}^N \|R(\theta_i)(\nabla m)_i\|_{\Sigma}^2 = \|D(\theta)m\|_2^2, \quad (11)$$

where $D(\theta)$, with $\theta = [\theta_1, \dots, \theta_N]^T$, represents the local anisotropic differential operator, given by

$$D(\theta) = \begin{pmatrix} I & 0 \\ 0 & \sqrt{\epsilon}I \end{pmatrix} \begin{pmatrix} C_\theta & S_\theta \\ -S_\theta & C_\theta \end{pmatrix} \begin{pmatrix} \nabla_x \\ \nabla_z \end{pmatrix}. \quad (12)$$

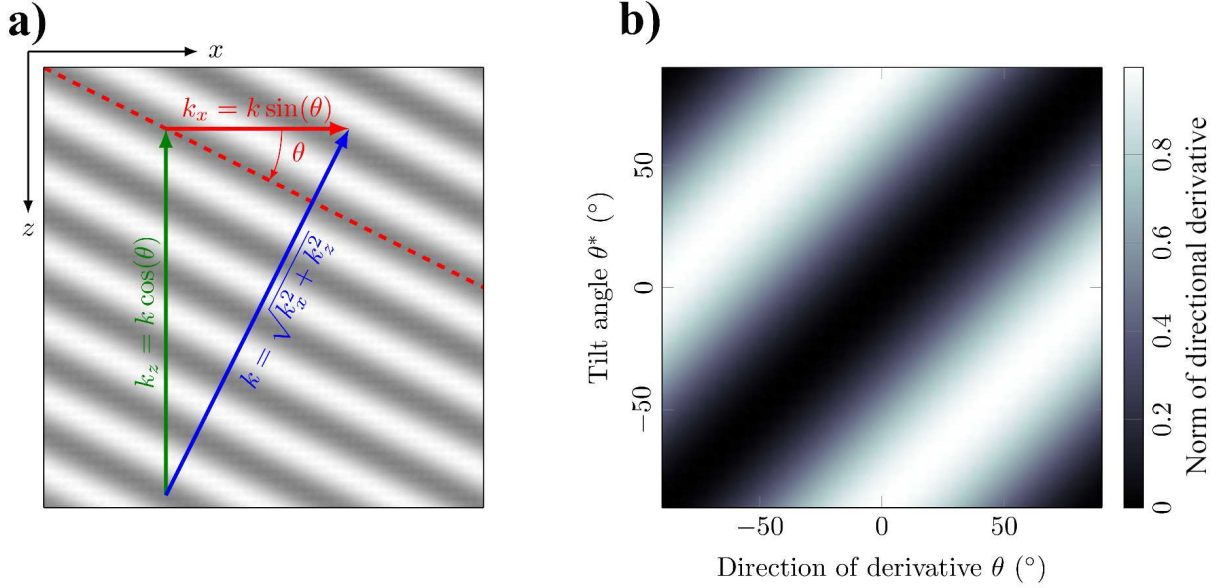


Figure 1: (a) A 2D sinusoidal plane wave $m(x, z) = \cos(k_x x - k_z z) := \cos(k \sin(\theta)x - k \cos(\theta)z)$ described by the tilt angle pointing in the direction of zero data gradient (constant phase), perpendicular to the wavenumber k that is in the direction of highest data gradient (maximum phase). (b) Norm of directional derivative $\|\nabla_{\theta} \cos(k \sin(\theta^*)x - k \cos(\theta^*)z)\|_2^2$ as a function of the signal tilt and the direction of derivative.

Here C_{θ} and S_{θ} denote diagonal matrices with $\cos \theta$ and $\sin \theta$ on their main diagonal, respectively. Therefore, the minimization problem in equation 6 is quadratic with respect to m . Applying the optimality conditions leads us to the following expression for the updated model parameters:

$$m^+ = (\mu G^T G + D(\theta)^T D(\theta))^{-1} (\mu G^T d). \quad (13)$$

2.2 Solving the Tilt Subproblem in equation 7

The problem in equation 7 is a constrained nonconvex and nonlinear optimization problem with respect to θ , thus iterative gradient-based methods can be employed to (locally) solve it. Introducing the auxiliary variable z , the constraint $z = \theta$, and the Lagrange multiplier vector λ , the ADMM [3, 18, 30] leads to the following iteration (see Appendix B):

$$\theta^+ = (J(m^+, \theta)^T J(m^+, \theta) + \tau I + \rho \nabla^T \nabla)^{-1} g(m^+, \theta, z, \lambda), \quad (14a)$$

$$z^+ = \min(\max(\theta^+ - \lambda, -\frac{\pi}{2}), \frac{\pi}{2}), \quad (14b)$$

$$\lambda^+ = \lambda - \tau(\theta^+ - z^+), \quad (14c)$$

where $J(m, \theta)$ denotes the Jacobian of $D(\theta)m$, the triplet (θ, z, λ) are the values at the current iteration, $(\theta^+, z^+, \lambda^+)$ are the updated values, and τ is the penalty parameter.

2.3 Selection of the regularization parameters

The parameters μ , ρ , and τ should be properly set for the proposed algorithm to produce meaningful results. We dynamically tune the value of these parameters during the iterations.

Regarding the regularization parameter μ for anisotropic Tikhonov regularization applied to the model parameters m , we assume that a good estimate of the data error bound ε , defined as

$$\|Gm - d\|_2^2 = \varepsilon, \quad (15)$$

is available. This allows us to update μ by a fixed-point iteration solving for the constraint in equation 15:

$$\mu^+ = \frac{2\|Gm^+ - d\|_2^2}{\|Gm^+ - d\|_2^2 + \varepsilon} \mu, \quad (16)$$

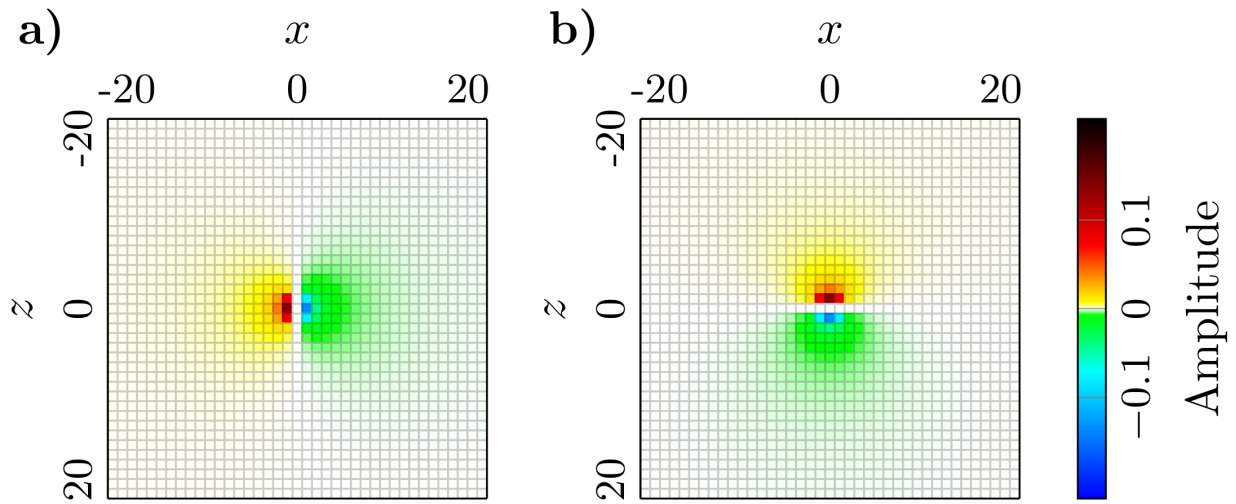


Figure 2: The 2D Hilbert transform filters in (a) the horizontal direction and (b) the vertical direction.

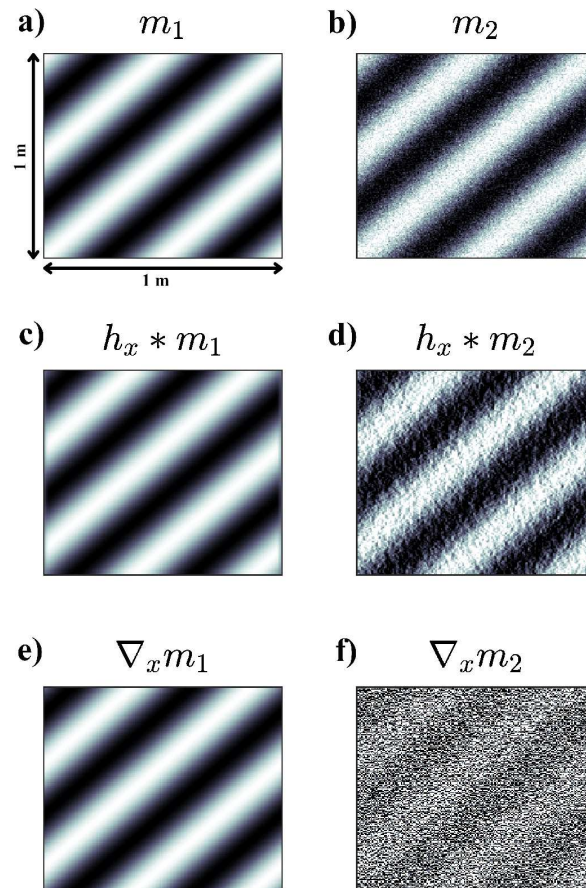


Figure 3: Comparison of signal derivatives calculated using the Hilbert transform filter (c-d) and standard finite differences (e-f) applied to a sinusoidal plane wave with and without added random noise (a-b).

where μ^+ is the updated parameter and m^+ is the model obtained by using the current parameters (μ, ρ, τ) ; see Gholami and Gazzola [19].

Choosing an optimal value for the regularization parameter for the tilt field ρ is challenging. While this paper does not aim to provide a method for selecting an optimal value for ρ , a practical approach is offered to simplify the search. At each iteration, ρ is set proportionally to the maximum value of the vector $\text{diag}(J^T J)$, ensuring reasonable smoothness of the tilt field and minimization of the first term in the anisotropic regularization term. Specifically

$$\rho = \epsilon_1 \max(\text{diag}(J^T J)), \quad (17)$$

where ϵ_1 is a positive parameter.

The parameter τ is associated to the ADMM method used to solve the optimization problem defined in equation 7, and serves as a penalty parameter enforcing the tilt field to lie between $-\pi/2$ and $\pi/2$. At each iteration, its value is set proportional to the maximum value of the vector $\text{diag}(J^T J)$, achieving a reasonable damping towards the box constraint and minimizing the first term in the anisotropic regularization term. Specifically:

$$\tau = \epsilon_2 \max(\text{diag}(J^T J)), \quad (18)$$

where ϵ_2 is a positive parameter.

For the 2D numerical examples in this paper, we use $\epsilon_1 = 1$ and $\epsilon_2 = 0.1$.

The proposed algorithm for 2D problems is summarized in Algorithm 1.

Algorithm 1: Local anisotropic regularization with tilt estimation in 2D space.

Inputs: data d , forward operator G , initial penalty parameter μ , ϵ_1 , and ϵ_2 .

Set $\theta = z = \lambda = 0$.

while a stopping criterion is not satisfied **do**

$$m \leftarrow (\mu G^T G + D(\theta)^T D(\theta))^{-1} (\mu G^T d)$$

for $k = 1, \dots, K$ **do**

$$\theta \leftarrow (J(m, \theta)^T J(m, \theta) + \tau I + \rho \nabla^T \nabla)^{-1} g(m, \theta, z, \lambda)$$

$$z \leftarrow \min(\max(\theta - \lambda, -\frac{\pi}{2}), \frac{\pi}{2})$$

$$\lambda \leftarrow \lambda - \tau(\theta - z)$$

end

$$\mu \leftarrow \frac{2 \|Gm - d\|_2^2}{\|Gm - d\|_2^2 + \epsilon} \mu$$

end

Outputs: model m and tilt field θ

3 3D anisotropic regularization

Navigating orientation in 3D space is naturally more difficult than in 2D, where a single parameter, the tilt θ , may simply specify the orientation of linear events (see Figure 1). To deal with this complication, we use a right-handed coordinate system, with the x axis extending forward, the y axis pointing rightward, and the z axis downward (see Figure 4).

In 3D space, the directional derivative of the model m in the direction of a vector

$$x'(\alpha, \beta, \gamma) = [\cos \alpha, \cos \beta, \cos \gamma], \quad (19)$$

takes the form:

$$\nabla_{x'} m = m_x \cos \alpha + m_y \cos \beta + m_z \cos \gamma = x'(\alpha, \beta, \gamma) \cdot \nabla m, \quad (20)$$

where α, β , and γ denote the direction angles formed by the vector and the positive x, y , and z axes, respectively, \cdot denotes the Euclidean inner product in \mathbb{R}^3 , and $\nabla m = [m_x, m_y, m_z]^T$. These angles offer a comprehensive means of characterizing the direction of vectors in 3D space. We simplify our notation to align with geology and geophysics

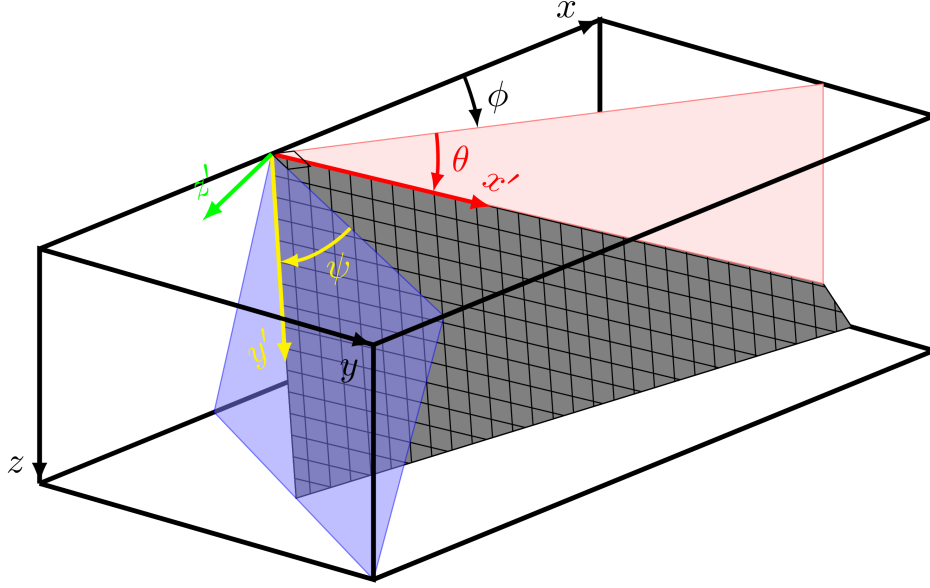


Figure 4: Quantities from mathematics and geology used to specify the orientation of linear and planar events in 3D space. A linear event (shown by the vector x') is mathematically determined by the two angles strike (ϕ) and tilt (θ). The tilt (θ) represents the angle, measured from the horizon, of the direction of maximum coherency in the vertical plane (in red) of the strike angle (ϕ), which is measured from the positive x axis. The dip (ψ) is the angle measured from the horizon of the maximum coherency (shown by the vector y') in a plane (in blue) perpendicular to x' . Planar events as formed by two vectors x' and y' and are determined by three angles (ϕ, θ, ψ).

conventions by using two independent angles, the strike (ϕ) and tilt (θ), derived from the spherical coordinate system. These angles relate to the direction angles as follows (using the relation between direction cosines):

$$\begin{cases} \cos \alpha = \cos \theta \cos \phi, \\ \cos \beta = \cos \theta \sin \phi, \\ \cos \gamma = \sin \theta. \end{cases} \quad (21)$$

These relations facilitate a more consistent notation between our 2D and 3D formulations and within the context of geology and geophysics, although alternative relations are also possible, leading to different conventions.

Figure 4 shows a tilted vector x' , representing a linear event in a dipping plane contained in the model, and the angles ϕ and θ . The strike angle ϕ , measured from the positive x axis, specifies the direction of the vertical plane that includes the tilt vector and θ is the inclination angle of the vector from the horizon. By using these new angles we rewrite the directional derivative in equation 20 as

$$\nabla_x m = m_x \cos \theta \cos \phi + m_y \cos \theta \sin \phi + m_z \sin \theta.$$

Similar to the 2D case we can determine the local dip and local strike angles at each point of a 3D model by minimizing $\|\nabla_{x'} m\|_2^2$. However, we can only use this equation to find the direction of greatest coherence in a sphere centered at each point. This only determines linear events in 3D space and thus cannot determine the orientation of the 2D planar features. To do this we need also to specify linear events in the direction perpendicular to the direction

$$x'(\phi, \theta) = (\cos \theta \cos \phi, \cos \theta \sin \phi, \sin \theta). \quad (22)$$

This necessitates calculating the derivative orthogonal to x' and searching for the maximum coherence in the plane perpendicular to this direction (the blue plane in Figure 4). As a result, the first step is to specify the plane perpendicular to x' . This can be accomplished in a variety of ways. The most basic one is to use the Euler angle system. The vector x' in Figure 4 can be expressed in a rotated coordinate system created by rotating the original coordinate system about the z axis by ϕ and then rotating the outcomes about the y axis by θ . These rotations can be performed using the 3×3 rotation matrices $R_y(\theta)$ and $R_z(\phi)$ defined as

$$R_y(\theta) = \begin{pmatrix} \cos \theta & 0 & \sin \theta \\ 0 & 1 & 0 \\ -\sin \theta & 0 & \cos \theta \end{pmatrix}, \quad (23)$$

and

$$R_z(\phi) = \begin{pmatrix} \cos \phi & \sin \phi & 0 \\ -\sin \phi & \cos \phi & 0 \\ 0 & 0 & 1 \end{pmatrix}, \quad (24)$$

giving the total rotation matrix

$$R_y(\theta)R_z(\phi) = \begin{pmatrix} \cos \theta \cos \phi & \cos \theta \sin \phi & \sin \theta \\ -\sin \phi & \cos \phi & 0 \\ -\sin \theta \sin \phi & -\sin \theta \cos \phi & \cos \theta \end{pmatrix}.$$

As can be seen, the first row of this matrix provides the desired direction x' , and because the rotation matrices are orthonormal, the second and third rows of this matrix form the basis for the desired plane perpendicular to x' . This plane can be rotated using the rotation matrix

$$R_x(\psi) = \begin{pmatrix} 1 & 0 & 0 \\ 0 & \cos \psi & \sin \psi \\ 0 & -\sin \psi & \cos \psi \end{pmatrix}. \quad (25)$$

The rotation angle ψ is clockwise about the x' axis. The total rotation matrix is defined by

$$\begin{aligned} R(\phi, \theta, \psi) &= R_x(\psi)R_y(\theta)R_z(\phi) := \begin{pmatrix} x'(\phi, \theta, \psi) \\ y'(\phi, \theta, \psi) \\ z'(\phi, \theta, \psi) \end{pmatrix} \\ &= \begin{pmatrix} \cos \theta \cos \phi & \cos \theta \sin \phi & \sin \theta \\ -\cos \psi \sin \phi - \sin \psi \sin \theta \cos \phi & \cos \psi \cos \phi - \sin \psi \sin \theta \sin \phi & \sin \psi \cos \theta \\ \sin \psi \sin \phi - \cos \psi \sin \theta \cos \phi & -\cos \psi \sin \phi - \cos \psi \sin \theta \sin \phi & \cos \psi \cos \theta \end{pmatrix}. \end{aligned} \quad (26)$$

In this formulation, the rotated coordinate system (x', y', z') is obtained by rotating the original coordinate system (x, y, z) using three successive rotations $R_z(\phi)$, $R_y(\theta)$, and $R_x(\psi)$. In this notation, the tilt (θ) represents the angle, measured from the horizontal, of the direction of maximum coherency in the vertical plane of the strike angle (ϕ), which is measured from the positive x axis. On the other hand, the dip (ψ) is the angle, measured from the horizontal, of the maximum coherency in a plane perpendicular to the direction of maximum coherency.

We define the local anisotropic regularization term for 3D problems using the 3D rotation matrix in equation 26 as

$$\sum_{i=1}^N \|R(\phi_i, \theta_i, \psi_i)(\nabla m)_i\|_{\Sigma_i}^2, \quad (27)$$

where

$$(\nabla m)_i = \begin{pmatrix} (\nabla_x m)_i \\ (\nabla_y m)_i \\ (\nabla_z m)_i \end{pmatrix}, \quad \Sigma_i = \begin{pmatrix} \sigma_x & 0 & 0 \\ 0 & \sigma_y & 0 \\ 0 & 0 & \sigma_z \end{pmatrix}. \quad (28)$$

The degree of anisotropy in our regularization is controlled through the parameters $\sigma_x \geq \sigma_y \geq \sigma_z \geq 0$ for every point in the domain (so that $\Sigma_i = \Sigma$). These parameters can be adjusted individually for each point in the model, as demonstrated by Lavielle et al. [24]. However, for the sake of simplicity and to maintain consistency, we employ fixed values throughout this paper. Without any loss of generality, we set $\sigma_x = 1$, $\sigma_y = \delta$, and $\sigma_z = \epsilon$, where $1 > \delta > \epsilon$, with $\epsilon \ll 1$. This specific configuration enforces a preference for planar-like and line-like structures within the model. In this case, the unit vector z' will indicate the directions with the highest model gradients while the unit vector x' will indicate the directions with the lowest model gradients, aligned along linear features. The unit vector y' will indicate the directions with intermediate data gradients. Planar features in the model will be explained by the $x'y'$ plane. Figure 5 depicts an anisotropy ellipsoid at a model point. The highest degree of anisotropy occurs when $\sigma_y = \sigma_z = 0$, resulting in a needle-shaped ellipsoid that favors models with elongated features aligned with the x' direction. In the case of isotropy, where all parameters are set to unity, the regularization behaves spherically.

Similarly to the 2D case, to address 3D linear inverse problems we regularize the associated linear system $Gm = d$ using a local anisotropic Tikhonov method. Given an initial guess (ϕ, θ, ψ) for the orientation parameters, this method employs a two-step iterative procedure that sequentially estimates both the model parameters and the orientation parameters as follows

$$m^+ = \underset{m}{\operatorname{argmin}} \frac{\mu}{2} \|Gm - d\|_2^2 + \frac{1}{2} \sum_{i=1}^N \|R(\phi_i, \theta_i, \psi_i)(\nabla m)_i\|_{\Sigma_i}^2, \quad (29)$$

$$\begin{aligned} \begin{pmatrix} \phi^+ \\ \theta^+ \\ \psi^+ \end{pmatrix} &= \arg \min_{(\phi, \theta, \psi) \in B} \frac{1}{2} \sum_{i=1}^N \|R(\phi_i, \theta_i, \psi_i)(\tilde{\nabla} m^+)_i\|_{\Sigma}^2 \\ &+ \frac{\rho_\phi}{2} \|\nabla \phi\|_2^2 + \frac{\rho_\theta}{2} \|\nabla \theta\|_2^2 + \frac{\rho_\psi}{2} \|\nabla \psi\|_2^2. \end{aligned} \quad (30)$$

Here $\rho_\psi, \rho_\phi, \rho_\theta$ are positive parameters controlling the smoothness of the estimated dip, strike, and tilt fields, and $B = (-\pi/2, \pi/2]^3$. As in the 2D case, $\tilde{\nabla} m$ represents a smoothed (regularized) estimate of the model gradient ∇m . We achieve this by smoothing the gradient components, $\tilde{m}_x = \tilde{\nabla}_x m$, $\tilde{m}_y = \tilde{\nabla}_y m$ and $\tilde{m}_z = \tilde{\nabla}_z m$, using 3D smooth derivative filters h_x, h_y and h_z :

$$\tilde{m}_x = h_x \star m, \quad \tilde{m}_y = h_y \star m, \quad \tilde{m}_z = h_z \star m, \quad (31)$$

with the generalized 3D Hilbert (Riesz) transform filters

$$\begin{aligned} h_x &= -\frac{1}{\pi^2} \frac{x}{(x^2 + y^2 + z^2)^2}, \\ h_y &= -\frac{1}{\pi^2} \frac{y}{(x^2 + y^2 + z^2)^2}, \\ h_z &= -\frac{1}{\pi^2} \frac{z}{(x^2 + y^2 + z^2)^2}. \end{aligned} \quad (32)$$

3.1 Solving the Model Subproblem in equation 29

Applying the optimality conditions gives

$$m = (\mu G^T G + D(\phi, \theta, \psi)^T D(\phi, \theta, \psi))^{-1} (\mu G^T d), \quad (33)$$

where $D(\phi, \theta, \psi)$ is the 3D local anisotropic differential operator

$$D(\phi, \psi, \theta) = \begin{pmatrix} I & 0 & 0 \\ 0 & \sqrt{\delta} I & 0 \\ 0 & 0 & \sqrt{\epsilon} I \end{pmatrix} \begin{pmatrix} C_\theta C_\phi & C_\theta S_\phi & S_\theta \\ -C_\psi S_\phi - S_\psi S_\theta C_\phi & C_\psi C_\phi - S_\psi S_\theta S_\phi & S_\psi C_\theta \\ S_\psi S_\phi - C_\psi S_\theta C_\phi & -C_\psi S_\phi - C_\psi S_\theta S_\phi & C_\psi C_\theta \end{pmatrix} \begin{pmatrix} \nabla_x \\ \nabla_y \\ \nabla_z \end{pmatrix}. \quad (34)$$

Here C_\bullet and S_\bullet (with \bullet standing for ϕ, θ, ψ) are the diagonal matrices with $\cos(\bullet)$ and $\sin(\bullet)$ on their main diagonal.

3.2 Solving the Orientation-Parameters Subproblem in equation 30

Similarly to the 2D case discussed above, after introducing the auxiliary variables z_ϕ, z_θ, z_ψ and the constraints $z_\phi = \phi, z_\theta = \theta, z_\psi = \psi$, we employ the ADMM to solve equation 30 sequentially, with each angle updated independently at each iteration, as follows (see Appendix C):

$$\phi^+ = H_\phi(m^+, \phi, \theta, \psi)^{-1} g_\phi(m^+, \phi, \theta, \psi, z_\phi, \lambda_\phi), \quad (35a)$$

$$\theta^+ = H_\theta(m^+, \phi^+, \theta, \psi)^{-1} g_\theta(m^+, \phi^+, \theta, \psi, z_\theta, \lambda_\theta), \quad (35b)$$

$$\psi^+ = H_\psi(m^+, \phi^+, \theta^+, \psi)^{-1} g_\psi(m^+, \phi^+, \theta^+, \psi, z_\psi, \lambda_\psi), \quad (35c)$$

$$z_\phi^+ = \min(\max(\phi^+ - \lambda_\phi, -\frac{\pi}{2}), \frac{\pi}{2}), \quad (35d)$$

$$z_\theta^+ = \min(\max(\theta^+ - \lambda_\theta, -\frac{\pi}{2}), \frac{\pi}{2}), \quad (35e)$$

$$z_\psi^+ = \min(\max(\psi^+ - \lambda_\psi, -\frac{\pi}{2}), \frac{\pi}{2}), \quad (35f)$$

$$\lambda_\phi^+ = \lambda_\phi - \tau_\phi(\phi^+ - z_\phi^+), \quad (35g)$$

$$\lambda_\theta^+ = \lambda_\theta - \tau_\theta(\theta^+ - z_\theta^+), \quad (35h)$$

$$\lambda_\psi^+ = \lambda_\psi - \tau_\psi(\psi^+ - z_\psi^+), \quad (35i)$$

where \bullet (which stands for $\phi, \theta, \psi, z_\phi, z_\theta, z_\psi, \lambda_\phi, \lambda_\theta, \lambda_\psi$) are the values at the current iteration, \bullet^+ are the updated values, and $\tau_\phi, \tau_\theta, \tau_\psi$ are penalty parameters. The Hessian matrices H_ϕ, H_θ, H_ψ and right-hand-side vectors g_ϕ, g_θ, g_ψ are defined in equations 49 and 50, respectively.

3.3 Selection of the regularization parameters

The procedure outlined for selecting regularization parameters in the 2D case can be extended to the 3D algorithm. The parameter μ in equation 29 can be dynamically adjusted using equation 16. In each iteration, the regularization parameters ρ_\bullet and τ_\bullet , where \bullet represents ϕ , θ , and ψ , are set to be proportional to the maximum value of the diagonal of the associated Gauss-Newton Hessian $J_\bullet^T J_\bullet$, with the scale parameters ϵ_1 and ϵ_2 (see equations 17 and 18). For the numerical examples in this paper, we use $\epsilon_1 = 10$ and $\epsilon_2 = 0.1$.

The proposed algorithm for 3D problems is summarized in Algorithm 2.

Algorithm 2: Structural-orientation parameter estimation and local anisotropic regularization in 3D space.

Inputs: data d and forward operator G , and initial penalty parameter μ , ϵ_1 and ϵ_2 .

Set $\phi = \theta = \psi = z_\phi = z_\theta = z_\psi = \lambda_\phi = \lambda_\theta = \lambda_\psi = 0$.

while a stopping criterion is not satisfied **do**

$$m \leftarrow (\mu G^T G + D(\phi, \theta, \psi)^T D(\phi, \theta, \psi))^{-1} (\mu G^T d)$$

for $k = 1, \dots, K$ **do**

$$\phi \leftarrow H_\phi(m, \phi, \theta, \psi)^{-1} g_\phi(m, \phi, \theta, \psi, z_\phi, \lambda_\phi)$$

$$\theta \leftarrow H_\theta(m, \phi, \theta, \psi)^{-1} g_\theta(m, \phi, \theta, \psi, z_\theta, \lambda_\theta)$$

$$\psi \leftarrow H_\psi(m, \phi, \theta, \psi)^{-1} g_\psi(m, \phi, \theta, \psi, z_\psi, \lambda_\psi)$$

$$z_\phi \leftarrow \min(\max(\phi - \lambda_\phi, -\frac{\pi}{2}), \frac{\pi}{2})$$

$$z_\theta \leftarrow \min(\max(\theta - \lambda_\theta, -\frac{\pi}{2}), \frac{\pi}{2})$$

$$z_\psi \leftarrow \min(\max(\psi - \lambda_\psi, -\frac{\pi}{2}), \frac{\pi}{2})$$

$$\lambda_\phi \leftarrow \lambda_\phi - \tau_\phi(\phi - z_\phi)$$

$$\lambda_\theta \leftarrow \lambda_\theta - \tau_\theta(\theta - z_\theta)$$

$$\lambda_\psi \leftarrow \lambda_\psi - \tau_\psi(\psi - z_\psi)$$

end

$$\mu \leftarrow \frac{2\|Gm - d\|_2^2}{\|Gm - d\|_2^2 + \epsilon} \mu$$

end

Outputs: model m , tilt angles θ , strike angles ϕ , dip angles ψ

4 Numerical examples

In this section, we conduct a comprehensive experimental evaluation of the proposed local anisotropic regularization method coupled with structural-orientation parameter estimation, employing a variety of detailed 2D and 3D examples.

In our algorithms, there are two main iterations: the outer loop, which alternates between estimating the model and orientation parameter(s), and the inner loop, which iterates over the orientation parameter(s) for a given model. The outer loop continues until the change in successive model estimates and orientation parameter(s) estimate falls below a predefined threshold. The inner loop is characterized by the index k in Algorithms 1 and 2, and the maximum number of these iterations is denoted by K . For all the examples presented in this paper, we set $K = 1$. In each iteration of the algorithms, a set of linear systems associated with the model and with the orientation parameter(s) need to be solved. These systems are solved either by direct solvers for small to medium-sized problems or by an iterative solver like conjugate-gradient (CG) for larger problems. Our algorithms are not highly sensitive on the number of CG iterations, but these should nonetheless be appropriately set to ensure accurate solutions for the associated linear systems. In the 3D examples presented in this section, we stop the CG iteration either after reaching a maximum of 200 iterations or when the relative residual error falls below 10^{-4} .

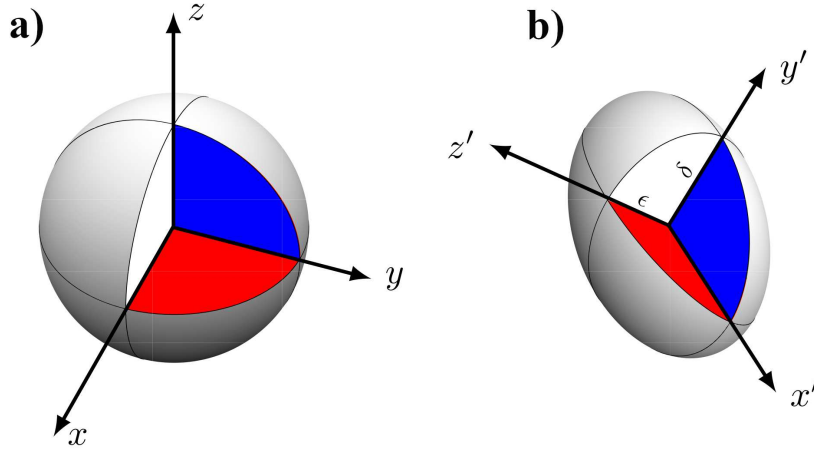


Figure 5: Ellipsoid representation of (a) isotropic and (b) anisotropic regularization in a 3D space.

4.1 2D examples: Simultaneous denoising and tilt estimation

4.1.1 Synthetic data

We start our investigation by addressing simultaneous denoising (with different signal-to-noise ratios) and tilt estimation, representing a crucial test for evaluating the performance of the proposed algorithm. Our choice of seismic data, illustrated in Figure 6a, comprises a synthetic model representing sedimentary layers featuring a plane unconformity and a curved fault, following the design by Fomel [15]. This model consists of 512 traces, each with 512 samples. To process this signal, we employ Algorithm 1 with $G = I$ (the identity matrix).

In the initial phase, we introduce no noise to the model, thereby setting a very low noise level ε to determine the regularization parameter for model reconstruction, as displayed in Figure 16. Figure 6b shows the estimated tilt field. The tilt angle is accurately determined at most points in the signal, except at positions corresponding to unconformities and faults, where the gradient is undefined. The value of the tilt angle at these positions is estimated based on a combination of neighboring points, the initial guess of the tilt, and the regularization applied during the estimation process. Figure 6c shows the corresponding convergence curve. These results demonstrate the algorithm’s remarkable speed and stability during convergence.

To assess the algorithm’s robustness, we introduce noise to the model shown in Figure 6a, targeting signal-to-noise ratios (S/N) of 20 dB, 10 dB, and 1 dB. After generating noisy data (Figure 7a-c), employing Algorithm 1 with a given noise level ε , we compute the denoised data (Figure 7d-f), and the estimated tilt fields (Figure 7g-i). For further insight, Figure 8a-c show a direct comparison of clean, noisy, and estimated signals for a specific trace segment in the middle of the section. We observe that, as the noise level increases, both the denoised signal and the estimated tilt become smoother; however, the continuous parts of the signal are less affected, thanks to the structure-oriented smoothing. This smoothing effect is more pronounced at unconformities and faults. Figures 8d-f show the corresponding convergence curves for the misfit function, penalty parameter μ , and regularization functional versus iteration, respectively. Although, in Figure 8d the misfit value (defined as $1/2\|d - m\|_2^2$) is reported for coherence with the metrics used later in this section to evaluate the performance of our method on other test problems, its final value in terms of S/N is 27 dB (for input S/N 20 dB), 22 dB (for input S/N 10 dB), 18 dB (for input S/N 1 dB). In Figure 9, the mean-squared error (MSE) is plotted for both the denoised signal and the estimated tilt field at different noise levels, utilizing the clean signal and its associated tilt field as reference benchmarks. In general, looking at Figures 7-9, we can conclude that our new algorithm exhibits high stability against varying noise levels.

As stated at the beginning of this section, the results presented so far are obtained using the parameters $\epsilon_1 = 1$ and $\epsilon_2 = 0.1$ when determining the regularization parameters ρ and τ through equations 17 and 18. To assess the algorithm’s sensitivity to these parameters, we conducted a test using a noisy signal with an S/N of 10 dB, as illustrated in the middle column of Figure 7. Algorithm 1 was run for simultaneous denoising and tilt estimation, employing different values for ϵ_1 and ϵ_2 . Figure 10 shows the MSE of the denoised signals. We observe that the algorithm is stable for a wide range of these parameters with greater sensitivity to the choice of ϵ_1 than ϵ_2 . This discrepancy arises from the fact that ϵ_2 governs the value of τ , imposing constraints on the tilt angles within the

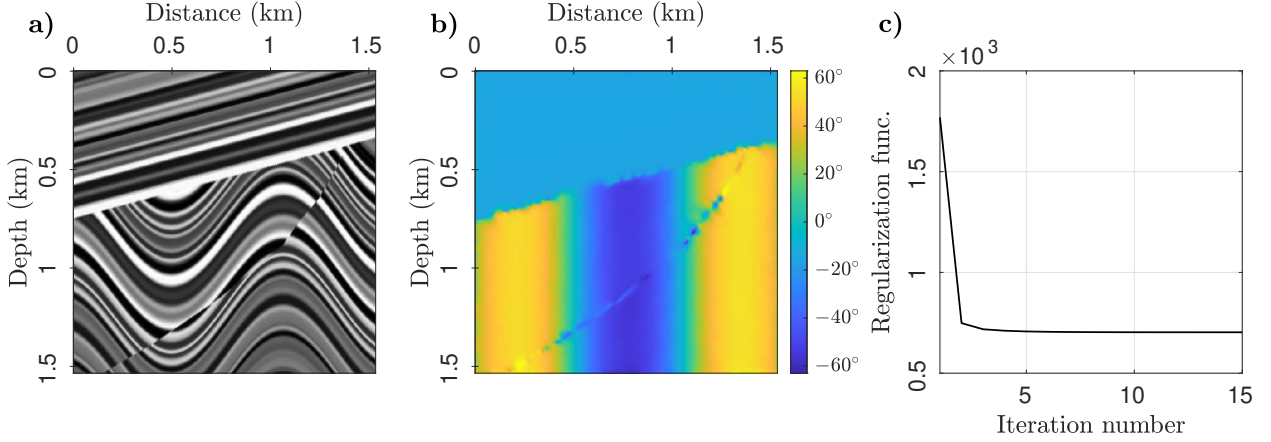


Figure 6: (a) Synthetic sedimentary model. (b) Tilt field estimation achieved through the proposed method. (c) Corresponding convergence curve depicting the algorithm’s stability and convergence characteristics.

range of $-\pi/2$ to $\pi/2$, but ϵ_1 enforces the degree of smoothness in the tilt field through the regularization parameters ρ . Although the corresponding reconstructions are not reported here, we observe that enforcing varying degrees of smoothness of the tilt field primarily affects the quality of estimate around the discontinuities.

4.1.2 Real data

Expanding our investigation to real seismic post-stack data, shown in Figure 11a, we consider complex structures associated with discontinues features. The data are from the North Viking Graben area of the North Sea and were published by ExxonMobil [23]. An interpretation of this data can be found in Madiba and McMechan [26]. The selected data region includes a complex toplap reflection package, including steeply dipping strata terminating against an overlying discontinuity surface, alongside nearly horizontal layers above. Such complex geological structures pose significant challenges for conventional isotropic denoising algorithms, which are typically equally smooth along every direction. We apply Algorithm 1 to denoise the seismic section, determining the noise level ϵ through trial and error-verified by observing the estimated noise becoming free of coherent energy. Figures 11b-d show the denoised section, the estimated noise, and the estimated tilt angle, respectively. The results show that, by employing anisotropic regularizers that act along the progressively estimated tilt field, the denoising is effective, preserving reflections while removing a significant portion of incoherent noise, as evident in Figure 11b. To provide further insight, Figure 12 tracks the evolution of the misfit function, penalty parameter μ , and regularization functional during iterations. These curves show the stability of the denoising algorithm in handling real seismic data containing complex structures such as discontinuities and steeply dipping layers. By effectively preserving discontinuities and reflections while suppressing noise, the algorithm enhances the interpretability of the data. This comprehensive analysis validates the ability of the algorithm to produce high-quality denoised sections, even when dealing with real seismic data featuring complex structures.

4.2 3D examples

4.2.1 3D synthetic Qdome model

In our examination of a 3D synthetic Qdome model, following Claerbout [11] and featuring complex structural elements such as curved events and faults (Figure 13a), we aim to evaluate the effectiveness of the proposed 3D algorithm in simultaneously denoising the data while estimating the structural orientation parameters, including dip, strike, and tilt. The model dimensions are 100 (inline traces) \times 100 (xline traces) \times 150 (time samples). For estimating the orientation parameters, we apply Algorithm 2 with the anisotropy parameters $\delta = 0.1$ and $\epsilon = 0$.

In a first instance, we do not add any noise to the model so that, given the clean nature of the model, we skip the model estimation subproblem (line 4) within Algorithm 2. This choice enabled us to evaluate the algorithm’s efficacy in denoising scenarios where the clean signal is not available, and orientation parameters need to be estimated simultaneously during the denoising process. To solve the linear systems with coefficient matrices H_\bullet appearing in equations 35a-35c, with $\bullet = \phi, \theta, \psi$, we employ the preconditioned CG iteration with diagonal preconditioner. Figures 13b-13d illustrate the obtained strike, tilt, and dip angles after 100 iterations of Algorithm 2. Examining the seismic signal in Figure 13a, we observe a downward bending of layers around 0.5 s along the positive spatial axes. Subsequently,

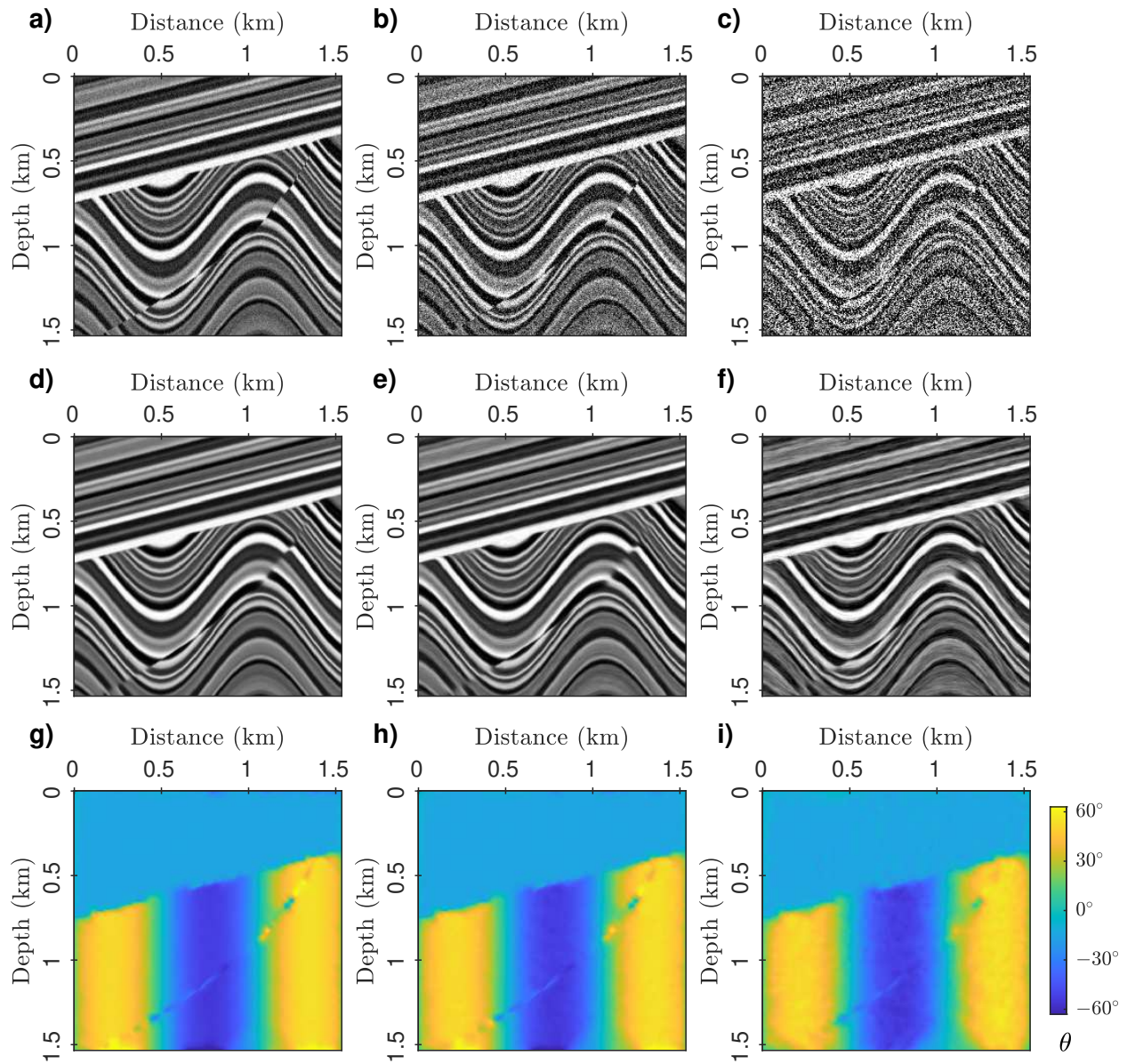


Figure 7: (a-c) Noisy signals with different signal-to-noise ratios: (a) S/N = 20 dB, (b) S/N = 10 dB, and (c) S/N = 1 dB. (d-f) Corresponding signals estimated using the anisotropic Tikhonov filter. (g-i) Corresponding estimated tilt fields.

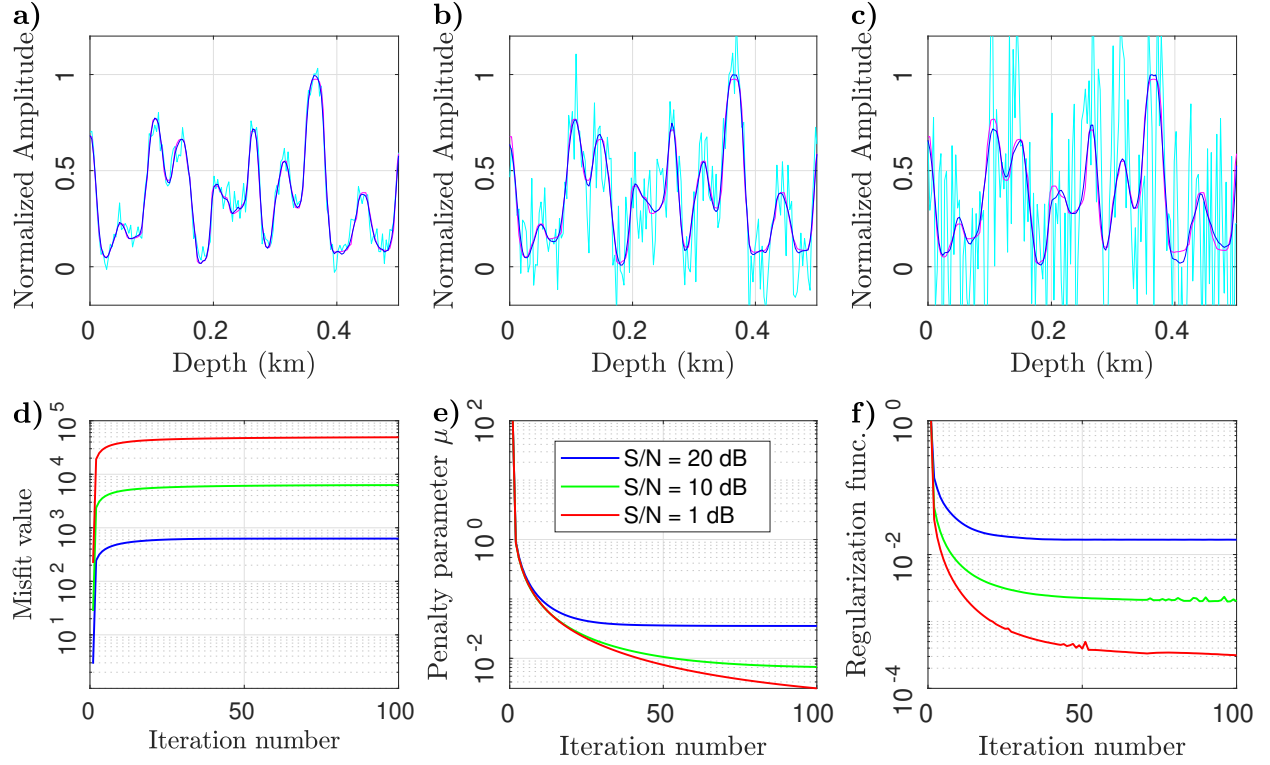


Figure 8: (a-c) A section (0 to 0.5 km) of the trace at a distance of 0.75 km for the denoising examples presented in Figure 7. Shown are (a) S/N = 20 dB, (b) S/N = 10 dB, and (c) S/N = 1 dB scenarios. In these panels, the true signal, noisy signal, and denoised signal are represented by magenta, cyan, and blue lines, respectively. (d-f) The evolution of key metrics: (d) Misfit function, (e) Penalty parameter, and (f) Regularization functional as a function of iteration.

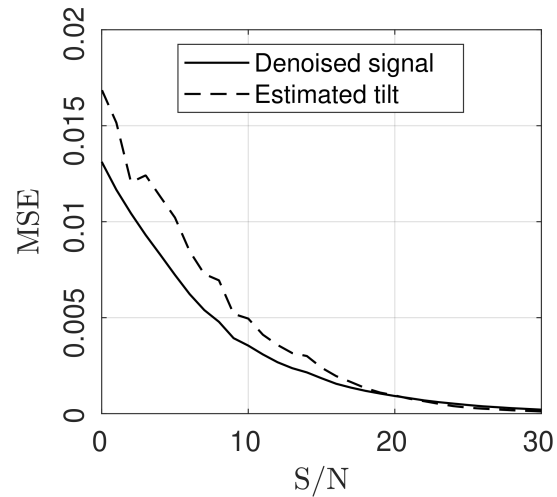


Figure 9: Performance evaluation of Algorithm 1 for simultaneous denoising and tilt estimation for different noise levels. The MSE is calculated for both the denoised signal and the estimated tilt field, using the clean signal and its associated tilt field as references for comparison.

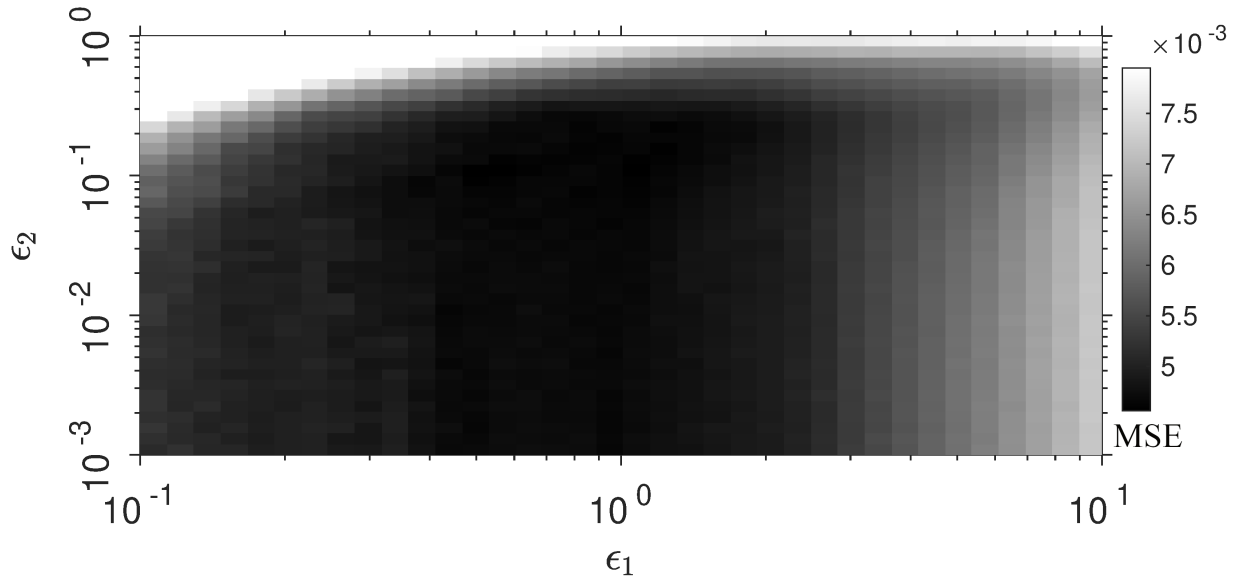


Figure 10: The MSE of Algorithm 1 for denoising a noisy signal with a S/N of 10 dB (shown in the middle column of Figure 7), with different values of the parameters ϵ_1 and ϵ_2 appearing in formulas 17 and 18 for the determination of the regularization parameter for tilt field estimation, and for the penalty parameters in ADMM.

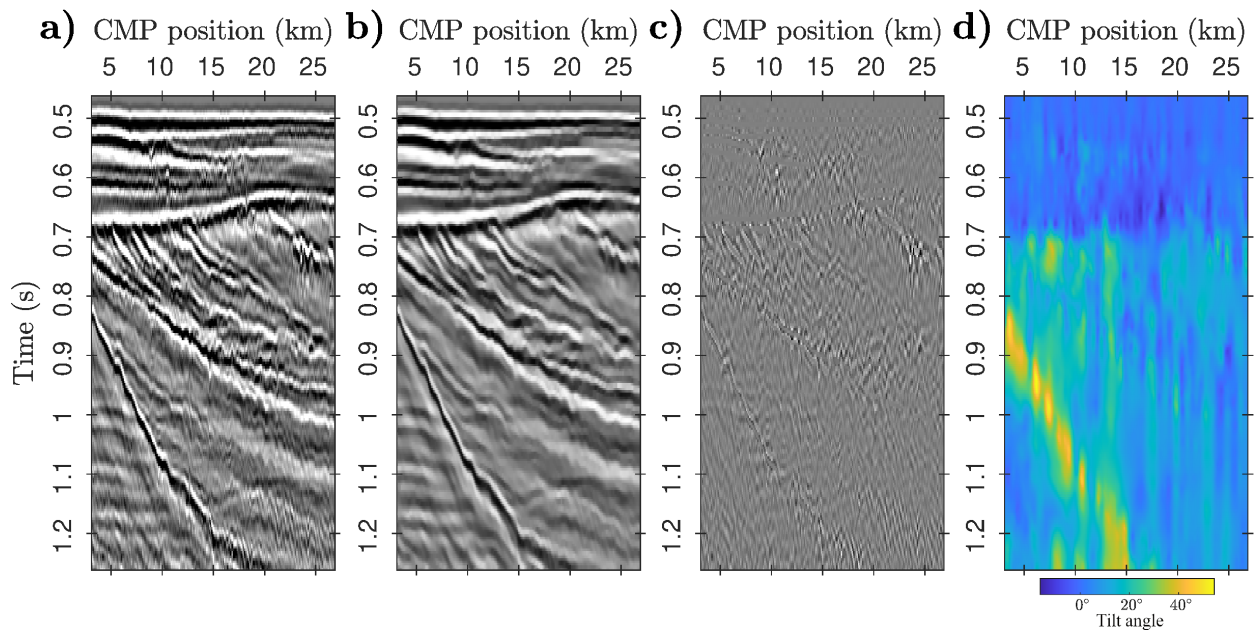


Figure 11: (a) Stack section of seismic field data. (b) Denoised section resulting from the application of Algorithm 1. (c) Section depicting the estimated noise. (d) Tilt field estimation. The progression of relevant optimization parameters is presented in Figure 12.

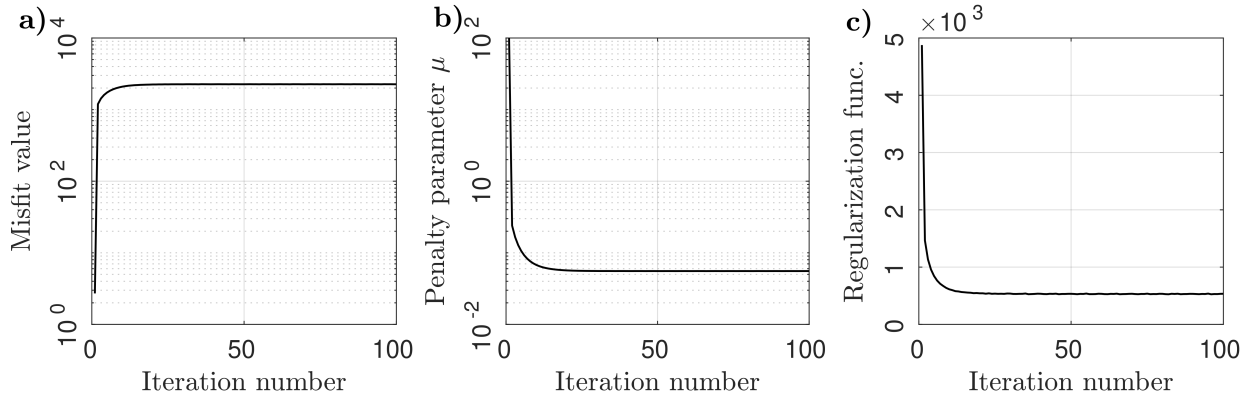


Figure 12: The evolution of crucial optimization parameters during the denoising process of the real seismic data presented in Figure 11. (a) shows the misfit function, (b) shows the penalty parameter, and (c) shows the regularization functional as a function of iteration.

the layers flatten around 1.1 s, followed by a reversal in bending direction down to 1.5 s. This characteristic behavior aligns well with the estimated tilt, as shown in Figure 13c, and dip angles in Figure 13d, with the dip angles slightly higher than the tilt. Additionally, it is noteworthy that, in this model, the layers’ strike, as depicted in Figure 13b, is quite high, ranging approximately between -60° and -20° . Figure 14 provides a graphical representation of the norm of directional derivatives. To emphasize the performance of the alternating direction minimization, we readdress the problem, focusing solely on the dip angle, assuming that the strike and tilt angles are known in advance (see Figures 13b-13c). The norm of derivatives in directions y' and z' , represented by dashed lines in Figure 14, highlights the convergence to the same solution, albeit with a difference in the convergence rate.

In a second instance, to make this problem more challenging, we add random noise with $S/N = 1$ dB to the model, as seen in Figure 15a. Employing Algorithm 2 and assuming knowledge of the noise level ε , we denoise the data effectively. Figures 15b and 15c present the denoised data and the noise that was successfully removed by the anisotropic filter after 200 iterations. Remarkably, the algorithm accurately attenuates the noise while preserving the intricate structural details within the data. The estimated strike, tilt, and dip angles are shown in Figures 15d and 15f. A direct comparison with the corresponding angles derived from clean data (Figures 13b-13d) shows the algorithm’s stability in the presence of noise in the input data. To provide insights into the algorithm’s convergence during the 3D denoising process illustrated in Figure 15, Figure 16 presents the evolution of various parameters across iterations.

4.2.2 3D field Parihaka data

In our assessment of the proposed algorithm’s performance, we use the Parihaka full-angle-stack seismic volume from New Zealand published by New Zealand Petroleum and Minerals. This dataset is freely accessible (<https://wiki.seg.org/wiki/Parihaka-3D>). We select a segment of the data characterized by dipping layers (Figure 17a). The chosen segment has dimensions of 201 (inline traces) \times 201 (xline traces) \times 101 (time samples). We initially employ Algorithm 2 to estimate the orientation parameters; the strike, tilt, and dip angles obtained after 20 iterations are displayed in Figures 17b-17d. Observing the time slice of the data (Figure 17a), we note that the layers are predominantly aligned along the (inline) x axis, a trend accurately captured in the strike field, displaying small angles between -8° and 0° (Figure 17b). Additionally, we observe that the layers are nearly horizontal in the time-inline section with a small positive tilt that increases with depth. This information is correctly reflected in the tilt field (Figure 17c), where the determined angles range between 0° and $+8^\circ$. As the layers exhibit more dip along the xline, as evident from the visible time-xline section of the data, we expect more dip angles than strike and tilt. This expectation is accurately represented in the dip field (Figure 17d), where the determined angles range between $+5^\circ$ and $+15^\circ$. Figure 18 shows the variation in the norm of directional derivatives. It is evident that the algorithm rapidly converges to a stationary point.

Finally, we harness local anisotropic regularization for a 3D missing trace interpolation experiment. This involved the random removal of 80% of the traces from the original Parihaka data volume, generating the missing data volume displayed in Figure 19a. The resulting interpolated data volume is illustrated in Figure 19b, while the associated error

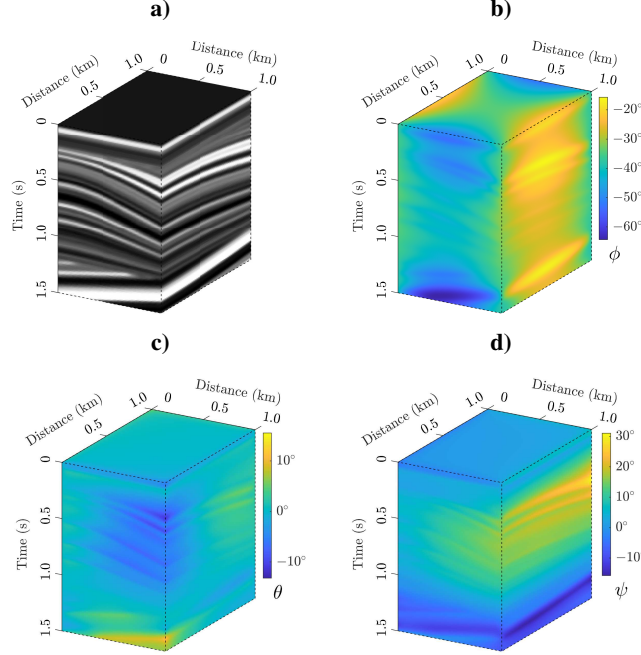


Figure 13: (a) 3D synthetic Qdome model. (b-d) Estimated orientation parameters, including (b) strike angle ϕ , (c) tilt angle θ , and (d) dip angle ψ .

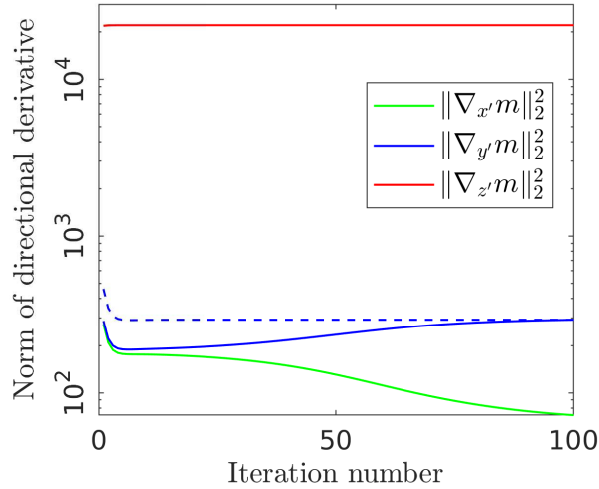


Figure 14: 3D synthetic Qdome model. Solid lines depict the progression of the norm of directional derivatives during the generation of Figure 13 using Algorithm 2. Dashed lines represent the norm of derivatives when fully minimizing $\|\nabla_{x'(\phi, \theta)} m\|_2^2$ at each iteration prior to updating the dip angle.

relative to the original data is shown in Figure 19c. Figures 19d-19f show the strike, tilt, and dip angles estimated throughout the interpolation process. To gain insights into the algorithm's performance under varying percentages of missing data, we applied the interpolation process with different levels of missing data. Figure 20 shows the MSE for both the interpolated data and the estimated orientation parameters at different missing data levels, ranging from 10% to 90%. The original full data and its associated angles from Figure 17 serve as reference benchmarks. The consistent trend of the error curves in Figure 20 indicates the algorithm stability in interpolation across different degrees of missing data.

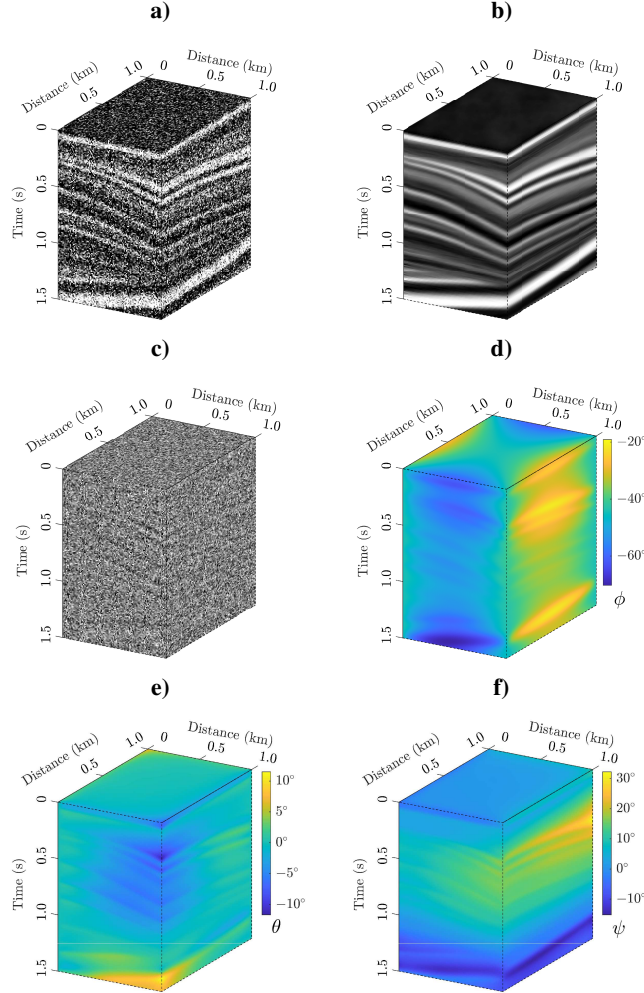


Figure 15: (a) Noisy 3D Qdome model. (b) Denoised model obtained through anisotropic Tikhonov filtering. (c) Estimated noise in the model. (d-f) Estimated orientation parameters, including (d) strike angle ϕ , (e) tilt angle θ , and (f) dip angle ψ . The evolution of relevant optimization parameters is presented in Figure 16.

5 Discussion

The introduction of local anisotropic regularization by Li and Oldenburg [25] and Clapp et al. [12] marked a significant advancement in geophysical inverse problems, allowing for the incorporation of geological information to ensure a unique and meaningful solution. Previous approaches operated under the assumption of a priori knowledge of orientation information, and often estimated such information separately before inversion using methods like filter techniques based on plane wave destruction. However, such approaches may encounter limitations when dealing with under-determined problems, where it is difficult to get a good estimate of the solution beforehand.

In this study, we relaxed this constraint by proposing a method that dynamically estimates orientation angles during the inversion process. This innovation offers two distinct advantages: firstly, anisotropic regularization becomes applicable to a wide range of problems, including under- and over-determined cases, and in any domain (time or depth). The required orientation parameters for designing the regularization function evolve adaptively with model estimation. Secondly, the recovered angles serve as a byproduct of the inversion, contributing valuable information for interpretation purposes.

Regularization primarily aims to suppress fluctuating, noise-like features in the estimated model that may arise from noise in the input data and the problem's ill-conditioning. Specifically, Tikhonov regularization in equation 2 incorporates prior assumptions about the desired solution's smoothness [22]. This is achieved using homogeneous smoothing

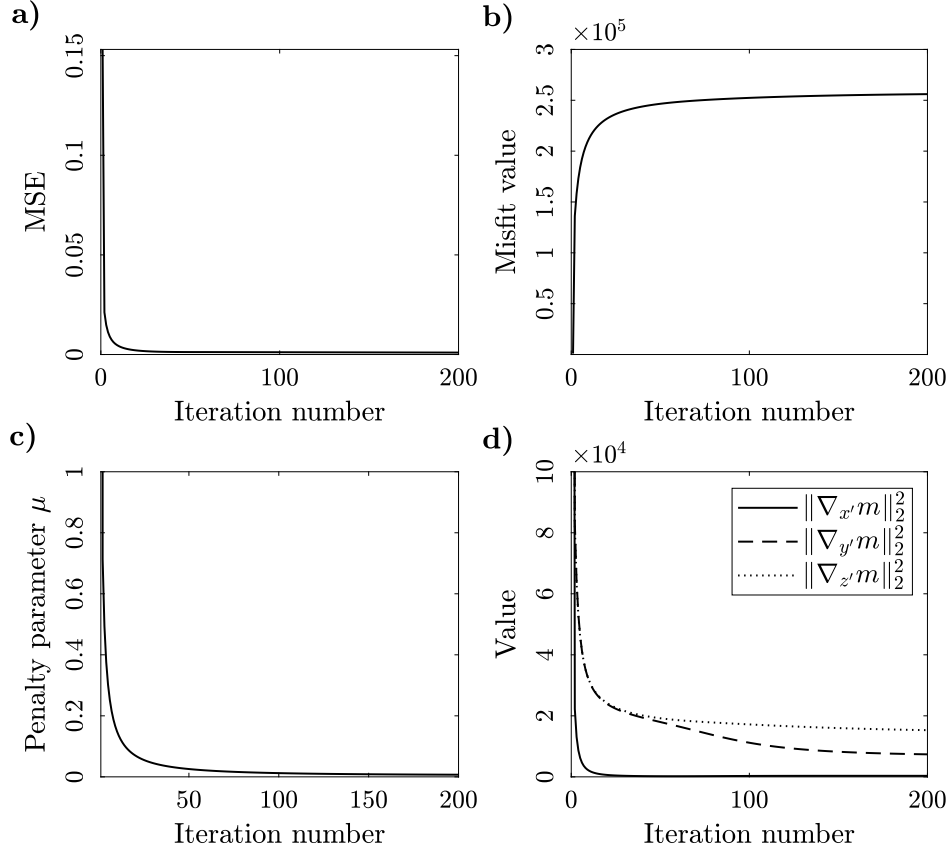


Figure 16: The evolution of key optimization parameters during the denoising process for the model shown in Figure 15b. Illustrated are (a) MSE, (b) the misfit function, (c) the penalty parameter μ , and (d) the norm of directional derivatives in the denoised model.

kernels, where each point in the model is computed with a weighted average of neighboring points, with weights decreasing as the distance from the target point increases. However, this traditional approach to regularization is somewhat naive as it does not consider the local structure of the model. In contrast, our proposed local anisotropic regularization adapts the shape of the smoothing kernel to apply smoothing along the structures present in the model. Namely, the adaptive smoothing kernels align with variations in the orientation and coherence paths of model features. Because signal variations are minimal along these coherence paths, the signal is preserved while noise is effectively canceled out through the averaging process of the kernel.

Numerous synthetic and field examples demonstrate that the new anisotropic regularization method provides solutions to geophysical inverse problems with high resolution and accurate representations of true structures. However, these advantages are accompanied by increased computational costs compared to standard isotropic regularization. Indeed, the latter just solves a problem expressed in the 2-norm (see equation 2, for which a direct solution method can be applied (although an iterative solver has to be adopted for large-scale problems)). The new alternating optimization framework for the model and orientation angles necessitates solving the original problem multiple times to refine the orientation parameter estimates gradually. However, this repeated solution of the model subproblem is also necessary in standard isotropic regularization to determine an appropriate value for the fitting parameter μ , following a continuation strategy [22]. Thus, the primary computational cost of our new algorithm for anisotropic regularization is the computation of the Tikhonov filter applied at each iteration (subproblem 14a for 2D problems and subproblems 35a-35c for 3D problems) to update the orientation parameters. Fortunately, the diagonal structure of the Jacobian matrix for these filters allows for efficient computation using standard linear algebra tools. The additional cost of the new approach compared to standard isotropic regularization is justified because, in addition to achieving higher quality reconstructions in practical applications, the regularization parameters are adaptively estimated.

The regularization parameter ρ plays a critical role in controlling the stationarity of the orientation angles, designing the regularization function. Proper selection of its value is crucial for the algorithm's convergence to a reasonable

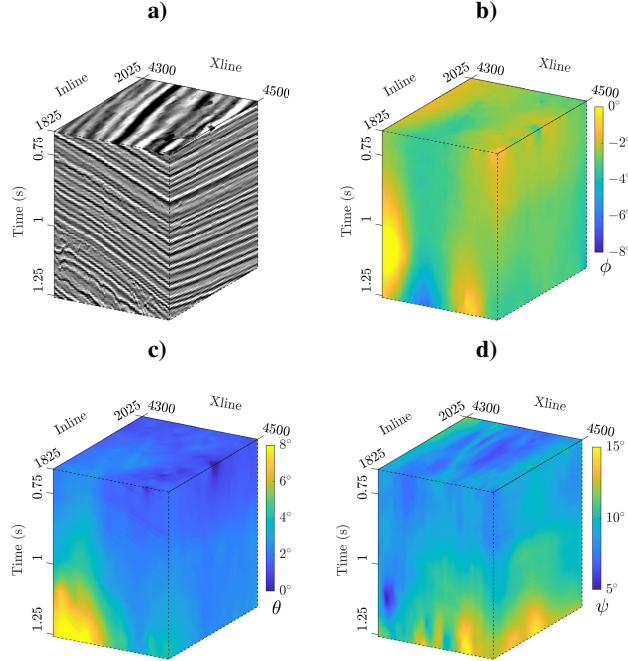


Figure 17: (a) 3D Parihaka field data. (b-d) estimated orientation parameters (b) strike angle ϕ , (c) tilt angle θ , and (d) dip angle ψ .

solution, particularly when dealing with underdetermined problems like trace interpolation. A recommended strategy is to initiate with a relatively large value for ρ or ϵ_1 and subsequently decrease it gradually throughout the iterations. While numerical results indicate the effectiveness of a fixed value of ρ , additional research is warranted to develop a robust algorithm for the automatic selection of ρ . Potential strategies include a robust continuation approach or integration of learning algorithms with training data [8].

The inherent ℓ_2 nature of the proposed anisotropic regularization may introduce some blurring effects in discontinuities such as faults and reflection terminations. This limitation could be mitigated adopting a number of alternative strategies, which extend the approach proposed in this paper. First, and most straightforwardly, one may be exploring alternative norms, such as the ℓ_1 -norm, leading to a directional total variation regularizer, which also allows us to recover discontinuities along the directions where regularization is applied. Second, one may consider locally adjusting the values for the anisotropy parameters σ_x , σ_y and σ_z , which automatically account for structures that may be more or less strongly aligned in the recovered directions. Third (generalizing the first and related to the second strategies), one may define a spatially varying norm regularization. For instance, employing an ℓ_p norm with spatially varying p (within the range of [1, 2]) could be considered, as in [21]. Such adaptive norm selection enables adjustments to the contribution of directional derivatives in the regularization term, potentially providing a more effective means of imposing smoothness and preserving discontinuities in the subsurface structure.

Finally, in this paper, we used the least-squares method to measure the data misfit, assuming that the noise in the data follows a Gaussian distribution. However, in practice, the data may be contaminated by outliers or erratic noises. In such cases, a robust error measure, such as the vector 1-norm, can be employed to impose smaller penalties on outliers.

6 Conclusions

In this paper we proposed a new method that allows us to simultaneously recover model and orientation parameters by applying local anisotropic Tikhonov regularization, where the latter are used to define an effective regularizer for the former. The method proved to be extremely valuable in a variety of test problems from geophysics. Future work will involve deriving strategies for selecting the regularization parameter ρ for the orientation parameters and extending the current approach to non-smooth regularizers, such as directional total variation (as explained in the previous section). Additionally, we aim to apply these methods to more challenging and potentially nonlinear problems, such as waveform inversion.

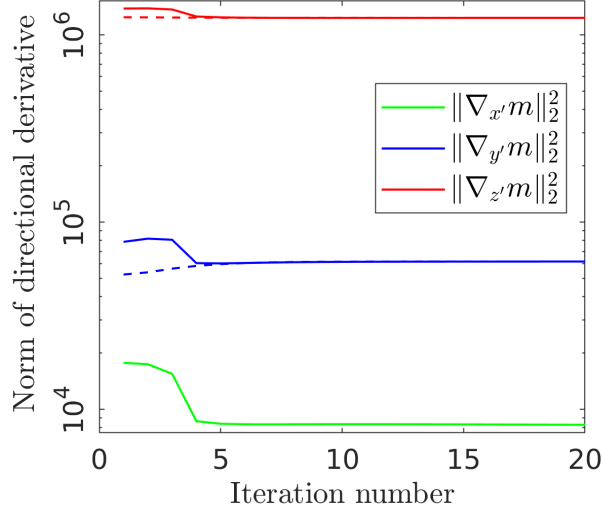


Figure 18: 3D Parihaka real data. Solid lines: evolution of the norm of directional derivatives in generating Figure 17 via Algorithm 2. Dashed lines: the norm of derivatives when fully minimizing $\|\nabla_{x'(\phi,\theta)} m\|_2^2$ at each iteration before updating the dip angle.

7 Appendix A: Estimation of the Orientation Parameter for a Plane Wave

Consider a 2D sinusoidal plane wave $m(x, z) = \cos(k_x x - k_z z)$ with $k_x = k \sin \theta^*$, $k_z = k \cos \theta^*$, $k = \sqrt{k_x^2 + k_z^2}$, and $\theta^* \in (-\frac{\pi}{2}, \frac{\pi}{2}]$ (see Figure 1). The gradient of $m(x, z)$ is

$$\begin{pmatrix} \partial_x m \\ \partial_z m \end{pmatrix} = \begin{pmatrix} -k_x \sin(k_x x - k_z z) \\ +k_z \sin(k_x x - k_z z) \end{pmatrix} = \begin{pmatrix} -c \sin \theta^* \\ c \cos \theta^* \end{pmatrix}, \quad (36)$$

where $c = k \sin(k_x x - k_z z)$. Without loss of generality, we assume $c = 1$. Consider the weighted norm

$$p(\theta) = \|\nabla_\theta m(x, z)\|_\Sigma^2 \quad (37)$$

of the directional derivative of $m(x, z)$ with respect to θ . By taking $\sigma_x = 1$ and $\sigma_z = 0$ we have

$$p(\theta) = (-\sin \theta^* \cos \theta + \cos \theta^* \sin \theta)^2, \quad (38)$$

whose first and second derivatives are

$$\frac{dp}{d\theta} = -\sin(2\theta^* - 2\theta), \quad \frac{d^2p}{d\theta^2} = 2 \cos(2\theta^* - 2\theta). \quad (39)$$

The first derivative vanishes at $\theta = \theta^* \pm n\frac{\pi}{2}$ for $n \in \mathbb{Z}$ (see again Figure 1). Furthermore, $\frac{d^2p}{d\theta^2} \geq 0$ for $\theta \in (\theta^* - \frac{\pi}{2}, \theta^* + \frac{\pi}{2})$, thus $p(\theta)$ is locally convex and gradient-based algorithms starting from $0 \in (\theta^* - \frac{\pi}{2}, \theta^* + \frac{\pi}{2})$ can converge to the true solution.

8 Appendix B: Tilt Estimation in 2D by ADMM

Here we provide the procedure for addressing the tilt estimation problem (as defined by equation 7) using ADMM. By introducing the auxiliary variable z , the constraint $z = \theta$, and the Lagrange multiplier vector λ , the ADMM formulation results in the following iterative scheme for estimating the tilt field θ associated with a given model m [see 3, 18, 30, for more details]

$$\begin{aligned} \theta^+ &= \arg \min_{\theta} \frac{1}{2} \sum_{i=1}^N \|R(\theta_i)(\tilde{\nabla} m)_i\|_\Sigma^2 + \frac{\rho}{2} \|\nabla \theta\|_2^2 \\ &\quad - \langle \lambda, \theta - z \rangle + \frac{\tau}{2} \|\theta - z\|_2^2, \end{aligned} \quad (40a)$$

$$z^+ = \min(\max(\theta^+ - \lambda, -\frac{\pi}{2}), \frac{\pi}{2}), \quad (40b)$$

$$\lambda^+ = \lambda - \tau(\theta^+ - z^+). \quad (40c)$$

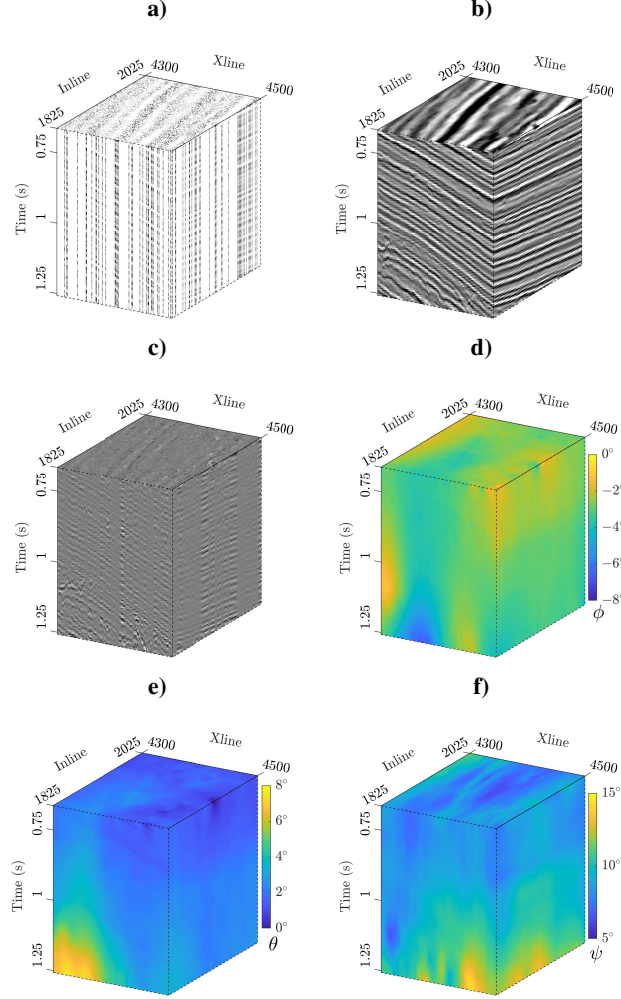


Figure 19: 3D field data interpolation example. (a) 3D Parihaka field data with 80% of the randomly chosen traces removed. (b) result of missing data interpolation by the 3D anisotropic Tikhonov regularization. (c) The difference between the reconstruction and the original data. (d-f) Estimated orientation parameters (d) strike angle ϕ , (e) tilt angle θ , and (f) dip angle ψ .

where the triplet (θ, z, λ) is the values at the current iteration, $(\theta^+, z^+, \lambda^+)$ are the updated values, and $\tau > 0$ is the penalty parameter.

We address the problem in equation 40a through a single iteration of the Gauss-Newton method. Noting that

$$\sum_{i=1}^N \|R(\theta_i)(\tilde{\nabla}m)_i\|_{\Sigma}^2 = \|\tilde{D}(\theta)m\|_2^2, \quad (41)$$

where \tilde{D} is defined as in equation 12, but computed with the smooth derivative operators $\tilde{\nabla}_x$ and $\tilde{\nabla}_z$, and assuming that the smooth derivative term $\tilde{D}(\theta)m$ is differentiable at θ , we can approximate it using the first two terms of a Taylor series expansion:

$$\tilde{D}(\underbrace{\theta + \delta\theta}_{\theta^+})m \approx \tilde{D}(\theta)m + \underbrace{\frac{\partial(\tilde{D}(\theta)m)}{\partial\theta}}_{J(m,\theta)} \delta\theta. \quad (42)$$

This gives the following closed form solution for the updated tilt field:

$$\theta^+ = (J(m,\theta)^T J(m,\theta) + \tau I + \rho \nabla^T \nabla)^{-1} g(m,\theta,z,\lambda), \quad (43)$$

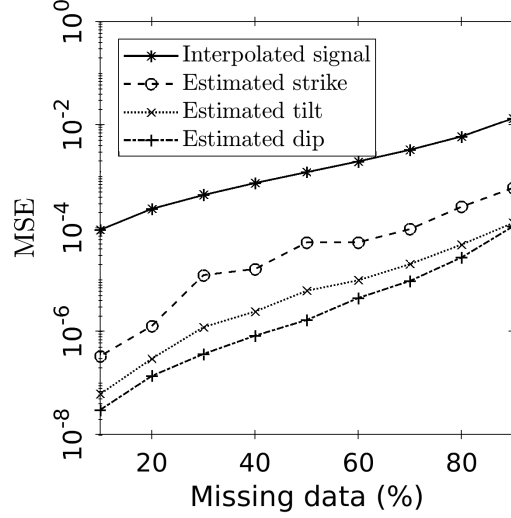


Figure 20: Performance evaluation of Algorithm 2 for simultaneous interpolation and estimation orientation parameters strike, tilt, and dip for different percents of missing data. The MSE is calculated using the original signal and its associated orientation parameters as references for comparison (Figure 17).

where J , the Jacobian matrix, and g are defined as:

$$J(m, \theta) = \begin{pmatrix} \text{diag}(\{\langle (\tilde{\nabla} m)_i, \frac{\partial x'(\theta_i)}{\partial \theta_i} \rangle\}_{i=1}^N) \\ \text{diag}(\{\langle \sqrt{\epsilon}(\tilde{\nabla} m)_i, \frac{\partial z'(\theta_i)}{\partial \theta_i} \rangle\}_{i=1}^N) \end{pmatrix}, \quad (44)$$

and

$$g(m, \theta, z, \lambda) = J(m, \theta)^T [J(m, \theta)\theta - \tilde{D}(\theta)m] + \tau z + \lambda. \quad (45)$$

9 Appendix C: Dip, Strike, and Tilt Estimation in 3D by ADMM

Similar to the 2D case discussed above, after introducing the auxiliary variables z_ϕ , z_θ , z_ψ and the constraints $z_\phi = \phi$, $z_\theta = \theta$, $z_\psi = \psi$, we employ ADMM to solve equation 30 sequentially, with each angle updated independently at each iteration, as follows:

$$\begin{aligned} \phi^+ = \arg \min_{\phi} & \frac{1}{2} \sum_{i=1}^N \|R(\phi_i, \theta_i, \psi_i)(\tilde{\nabla} m^+)_i\|_{\Sigma}^2 \\ & + \frac{\rho_\phi}{2} \|\nabla \phi\|_2^2 - \langle \lambda_\phi, \phi - z_\phi \rangle + \frac{\tau_\phi}{2} \|\phi - z_\phi\|_2^2 \end{aligned} \quad (46a)$$

$$\begin{aligned} \theta^+ = \arg \min_{\theta} & \frac{1}{2} \sum_{i=1}^N \|R(\phi_i^+, \theta_i, \psi_i)(\tilde{\nabla} m^+)_i\|_{\Sigma}^2 \\ & + \frac{\rho_\theta}{2} \|\nabla \theta\|_2^2 - \langle \lambda_\theta, \theta - z_\theta \rangle + \frac{\tau_\theta}{2} \|\theta - z_\theta\|_2^2 \end{aligned} \quad (46b)$$

$$\begin{aligned} \psi^+ = \arg \min_{\psi} & \frac{1}{2} \sum_{i=1}^N \|R(\phi_i^+, \theta_i^+, \psi_i)(\tilde{\nabla} m^+)_i\|_{\Sigma}^2 \\ & + \frac{\rho_\psi}{2} \|\nabla \psi\|_2^2 - \langle \lambda_\psi, \psi - z_\psi \rangle + \frac{\tau_\psi}{2} \|\psi - z_\psi\|_2^2 \end{aligned} \quad (46c)$$

$$z_\phi^+ = \min(\max(\phi^+ - \lambda_\phi, -\frac{\pi}{2}), \frac{\pi}{2}), \quad (46d)$$

$$z_\theta^+ = \min(\max(\theta^+ - \lambda_\theta, -\frac{\pi}{2}), \frac{\pi}{2}), \quad (46e)$$

$$z_\psi^+ = \min(\max(\psi^+ - \lambda_\psi, -\frac{\pi}{2}), \frac{\pi}{2}), \quad (46f)$$

$$\lambda_\phi^+ = \lambda_\phi - \tau_\phi(\phi^+ - z_\phi^+), \quad (46g)$$

$$\lambda_\theta^+ = \lambda_\theta - \tau_\theta(\theta^+ - z_\theta^+), \quad (46h)$$

$$\lambda_\psi^+ = \lambda_\psi - \tau_\psi(\psi^+ - z_\psi^+), \quad (46i)$$

where \bullet are the values at the current iteration, \bullet^+ are the updated values, and $\tau_\phi, \tau_\theta, \tau_\psi$ are penalty parameters.

Now, we explain how to solve subproblems 46a-46c. As for the 2D problems, we solve subproblems 46a-46c through a single iteration of the Gauss-Newton method. Noting that

$$\sum_{i=1}^N \|R(\phi_i, \theta_i, \psi_i)(\tilde{\nabla}m)_i\|_\Sigma^2 = \|\tilde{D}(\phi, \theta, \psi)m\|_2^2, \quad (47)$$

where \tilde{D} is defined as equation 34 but computed with the smooth derivative operator $\tilde{\nabla}$, and assuming that the smooth derivative term $\tilde{D}(\phi, \theta, \psi)m$ is differentiable at ϕ, θ, ψ , we can approximate it using the first two terms of a Taylor series expansion:

$$\begin{cases} \tilde{D}(\phi + \delta\phi, \theta, \psi)m \approx \tilde{D}(\phi, \theta, \psi)m + \frac{\partial(\tilde{D}(\phi, \theta, \psi)m)}{\partial\phi} \delta\phi, \\ \tilde{D}(\phi, \theta + \delta\theta, \psi)m \approx \tilde{D}(\phi, \theta, \psi)m + \frac{\partial(\tilde{D}(\phi, \theta, \psi)m)}{\partial\theta} \delta\theta, \\ \tilde{D}(\phi, \theta, \psi + \delta\psi)m \approx \tilde{D}(\phi, \theta, \psi)m + \frac{\partial(\tilde{D}(\phi, \theta, \psi)m)}{\partial\psi} \delta\psi. \end{cases}$$

This allows us to express the updated angles $\phi^+ = \phi + \delta\phi$, $\theta^+ = \theta + \delta\theta$ and $\psi^+ = \psi + \delta\psi$ in the following closed forms:

$$\phi^+ = H_\phi(m^+, \phi, \theta, \psi)^{-1} g_\phi(m^+, \phi, \theta, \psi, z_\phi, \lambda_\phi), \quad (48a)$$

$$\theta^+ = H_\theta(m^+, \phi^+, \theta, \psi)^{-1} g_\theta(m^+, \phi^+, \theta, \psi, z_\theta, \lambda_\theta), \quad (48b)$$

$$\psi^+ = H_\psi(m^+, \phi^+, \theta^+, \psi)^{-1} g_\psi(m^+, \phi^+, \theta^+, \psi, z_\psi, \lambda_\psi). \quad (48c)$$

In these equations, the Hessian matrices H_\bullet and right-hand-side vectors g_\bullet are defined as

$$H_\bullet(m, \phi, \theta, \psi) = J_\bullet(m, \phi, \theta, \psi)^T J_\bullet(m, \phi, \theta, \psi) + \tau_\bullet I + \rho_\bullet \nabla^T \nabla \quad (49)$$

and

$$g_\bullet(m, \phi, \theta, \psi, z, \lambda) = J_\bullet(m, \phi, \theta, \psi)^T [J_\bullet(m, \phi, \theta, \psi)\bullet - \tilde{D}(\phi, \theta, \psi)m] + \tau_\bullet z + \lambda, \quad (50)$$

respectively, where the Jacobian matrices J_\bullet are defined as:

$$J_\bullet(m, \phi, \theta, \psi) = \begin{pmatrix} \text{diag}(\langle (\tilde{\nabla}m)_i, \frac{\partial x'(\phi_i, \theta_i, \psi_i)}{\partial \bullet_i} \rangle) \\ \text{diag}(\langle \sqrt{\delta}(\tilde{\nabla}m)_i, \frac{\partial y'(\phi_i, \theta_i, \psi_i)}{\partial \bullet_i} \rangle) \\ \text{diag}(\langle \sqrt{\epsilon}(\tilde{\nabla}m)_i, \frac{\partial z'(\phi_i, \theta_i, \psi_i)}{\partial \bullet_i} \rangle) \end{pmatrix}. \quad (51)$$

Here \bullet stands for ϕ, θ and ψ .

10 ACKNOWLEDGMENTS

This research was partially funded by the SONATA BIS grant (No. 2022/46/E/ST10/00266) of the National Science Center in Poland.

References

- [1] Aster, R. C., B. Borchers, and C. H. Thurber, 2004, Parameter estimation and inverse problems: Academic Press.
- [2] Bakker, P., L. J. van Vliet, and P. W. Verbeek, 1999, Edge preserving orientation adaptive filtering: Proceedings. 1999 IEEE computer society conference on computer vision and pattern recognition (Cat. No PR00149), 535–540.

-
- [3] Boyd, S., N. Parikh, E. Chu, B. Peleato, and J. Eckstein, 2010, Distributed optimization and statistical learning via the alternating direction method of multipliers: *Foundations and trends in machine learning*, **3**, 1–122.
- [4] Chen, W., H. Wang, L. Yang, X. Liu, and Y. Chen, 2022, Nonstationary local slope estimation via forward-backward space derivative calculation: *Geophysics*, **87**, N1–N11.
- [5] Chen, Y., S. Zu, Y. Wang, and X. Chen, 2020, Deblending of simultaneous source data using a structure-oriented space-varying median filter: *Geophysical Journal International*, **222**, 1805–1823.
- [6] Chen, Z., S. Fomel, and W. Lu, 2013a, Accelerated plane-wave destruction: *Geophysics*, **78**, V1–V9.
- [7] Chen, Z., S. Fomel, and W. Lu, 2013b, Omnidirectional plane-wave destruction: *Geophysics*, **78**, V171–V179.
- [8] Chung, J., M. Chung, S. Gazzola, and M. Pasha, 2024, Efficient learning methods for large-scale optimal inversion design: *Numerical Algebra, Control and Optimization*, **14**, 137–159.
- [9] Claerbout, J. F., 1976, *Fundamentals of Geophysical Data Processing*: McGraw-Hill Book Co.
- [10] Claerbout, J. F., 1992, *Earth Sounding Analysis*: Blackwell Scientific Publications.
- [11] Claerbout, J. F., 1993, 3D local monoplane annihilator: SEP-77: Stanford Exploration Project, 19–25.
- [12] Clapp, R. G., B. L. Biondi, and J. F. Claerbout, 2004, Incorporating geologic information into reflection tomography: *Geophysics*, **69**, 533–546.
- [13] Clapp, R. G., B. L. Biondi, S. Fomel, and J. F. Claerbout, 1998, Regularizing velocity estimation using geologic dip information, *in* SEG Technical Program Expanded Abstracts 1998, 1851–1854. SEG.
- [14] Felsberg, M. and G. Sommer, 2000, A new extension of linear signal processing for estimating local properties and detecting features: *Mustererkennung 2000: 22. DAGM-Symposium*. Kiel, 13.–15. September 2000, 195–202.
- [15] Fomel, S., 2002, Applications of plane-wave destruction filters: *Geophysics*, **67**, 1946–1960.
- [16] Fomel, S., 2007, Velocity-independent time-domain seismic imaging using local event slopes: *Geophysics*, **72**, S139–S147.
- [17] Fomel, S. and A. Guitton, 2006, Regularizing seismic inverse problems by model reparameterization using plane-wave construction: *Geophysics*, **71**, A43–A47.
- [18] Gabay, D. and B. Mercier, 1976, A dual algorithm for the solution of nonlinear variational problems via finite element approximation: *Computers & mathematics with applications*, **2**, 17–40.
- [19] Gholami, A. and S. Gazzola, 2022, Automatic balancing parameter selection for Tikhonov-TV regularization: *BIT Numerical Mathematics*, **62**, 1873–1898.
- [20] Hale, D., 2009, Structure-oriented smoothing and semblance: CWP Report, 635.
- [21] Han, J. and Y. Lee, 2023, Inhomogeneous regularization with limited and indirect data: *Journal of Computational and Applied Mathematics*, **428**, 115193.
- [22] Hansen, C., 1998, Rank-deficient and discrete ill-posed problems - Numerical aspects of linear inversion: *Society for Industrial and Applied Mathematics - Mathematical modeling and computation*.
- [23] Keys, R. G. and D. J. Foster, 1998, Comparison of seismic inversion methods on a single real data set: SEG.
- [24] Lavialle, O., S. Pop, C. Germain, M. Donias, S. Guillon, N. Keskes, and Y. Berthoumieu, 2007, Seismic fault preserving diffusion: *Journal of Applied Geophysics*, **61**, 132–141.
- [25] Li, Y. and D. W. Oldenburg, 2000, Incorporating geological dip information into geophysical inversions: *Geophysics*, **65**, 148–157.
- [26] Madiba, G. B. and G. A. McMechan, 2003, Processing, inversion, and interpretation of a 2D seismic data set from the north viking graben, north sea: *Geophysics*, **68**, 837–848.
- [27] Marfurt, K. J., 2006, Robust estimates of 3D reflector dip and azimuth: *Geophysics*, **71**, P29–P40.
- [28] Merzlikin, D., S. Fomel, and X. Wu, 2020, Least-squares diffraction imaging using shaping regularization by anisotropic smoothing: *Geophysics*, **85**, S313–S325.
- [29] Schleicher, J., J. Costa, L. Santos, A. Novais, and M. Tygel, 2009, On the estimation of local slopes: *Geophysics*, **74**, P25–P33.
- [30] Tapia, R. A., 1977, Diagonalized multiplier methods and quasi-newton methods for constrained optimization: *Journal of Optimization Theory and Applications*, **22**, 135–194.
- [31] Tarantola, A., 2005, *Inverse Problem Theory and Methods for Model Parameter Estimation*: SIAM.
- [32] Wang, H., Y. Chen, O. M. Saad, W. Chen, Y. A. S. I. Oboué, L. Yang, S. Fomel, and Y. Chen, 2022, A MATLAB code package for 2D/3D local slope estimation and structural filtering: *Geophysics*, **87**, F1–F14.
- [33] Wu, X., 2017, Structure-, stratigraphy- and fault-guided regularization in geophysical inversion: *Geophysical Journal International*, **210**, 184–195.
- [34] Wu, X. and X. Jansson, 2017, Directional structure tensors in estimating seismic structural and stratigraphic orientations: *Geophysical Journal International*, **210**, 534–548.